METRICA
METRology Institutional CAtalog

ISTITUTO NAZIONALE DI RICERCA METROLOGICA
Repository Istituzionale

Cerium-, Europium- and Erbium-Modified ZnO and ZrO2 for Photocatalytic Water Treatment Applications: A Review

Original
Cerium-, Europium- and Erbium-Modified ZnO and ZrO2 for Photocatalytic Water Treatment Applications: A Review / Gaggero, Elisa; Calza, Paola; Cerrato, Erik; Paganini, Maria Cristina. - In: CATALYSTS. - ISSN 2073-4344. - 11:12(2021), pp. 1520-1575. [10.3390/catal11121520]

Availability:
This version is available at: 11696/73403 since: 2022-02-21T17:30:34Z

Publisher:
MDPI

Published
DOI:10.3390/catal11121520

Terms of use:

This article is made available under terms and conditions as specified in the corresponding bibliographic description in the repository

Publisher copyright

(Article begins on next page)

20 April 2025

catalysts

MDPI

Review

Cerium-, Europium- and Erbium-Modified ZnO and ZrO_2 for Photocatalytic Water Treatment Applications: A Review

Elisa Gaggero, Paola Calza, Erik Cerrato * and Maria Cristina Paganini

Dipartimento di Chimica and NIS, University of Turin, Via P. Giuria 7, 10125 Torino, Italy; elisa.gaggero@unito.it (E.G.); paola.calza@unito.it (P.C.); mariacristina.paganini@unito.it (M.C.P.)
* Correspondence: erik.cerrato@unito.it

Abstract: In the last decades photocatalysis has become one of the most employed technologies for the implementation of the so-called Advanced Oxidation Processes (AOPs) for the removal of harmful pollutants from wastewaters. The materials identified as the best photocatalysts are transition metal oxides, in which the band structure allows charge carrier separation upon solar irradiation. The photoinduced charge carrier can thus cause oxidative and reductive redox reactions at the surface, inducing the formation of the radical species able to initiate the AOPs. Despite the great advantages of this process (non-toxic, cheap and environmentally clean), the main drawback lies in the fact that the most efficient semiconductors are only able to absorb UV irradiation, which accounts for only 5% of the total solar irradiation at the Earth's surface and not enough to generate the required amount of electron-hole pairs. On the other hand, many efforts have been devoted to the sensitization of wide band gap transition metal oxides to visible light, which represents a higher percentage (almost 45%) in the solar electromagnetic spectrum. Among all the strategies to sensitize transition metal oxides to visible irradiation, doping with lanthanides has been less explored. In this regard, lanthanides offer a unique electronic configuration, consisting in 4f orbitals shielded by a 5s5p external shell. This occurrence, coupled with the different occupation of the localized 4f orbitals would provide an astounding opportunity to tune these materials' properties. In this review we will focus in depth on the modification of two promising photocatalytic transition metal oxides, namely ZnO and ZrO_2, with cerium, europium and erbium atoms. The aim of the work is to provide a comprehensive overview of the influence of lanthanides on the structural, optical and electronic properties of the modified materials, emphasizing the effect of the different 4f orbital occupation in the three considered doping atoms. Moreover, a large portion of the discussion will be devoted to the structural-properties relationships evidencing the improved light absorption working mechanism of each system and the resulting enhanced photocatalytic performance in the abatement of contaminants in aqueous environments.

Keywords: photocatalysis; water remediation; engineered transition metal oxides; visible light active systems; semiconductors; heterojunctions

check for updates

Citation: Gaggero, E.; Calza, P.; Cerrato, E.; Paganini, M.C. Cerium-, Europium- and Erbium-Modified ZnO and ZrO_2 for Photocatalytic Water Treatment Applications: A Review. *Catalysts* **2021**, *11*, 1520. https://doi.org/10.3390/catal11121520

Academic Editor: Daniela Nunes

Received: 22 November 2021
Accepted: 9 December 2021
Published: 14 December 2021

Publisher's Note: MDPI stays neutral with regard to jurisdictional claims in published maps and institutional affiliations.

Copyright: © 2021 by the authors. Licensee MDPI, Basel, Switzerland. This article is an open access article distributed under the terms and conditions of the Creative Commons Attribution (CC BY) license (https://creativecommons.org/licenses/by/4.0/).

1. Introduction

Water pollution arising from anthropogenic industrial contamination is one of the major challenges with which humanity will have to cope in the 21st century. In this regard, at least two of the seventeen Sustainable Development Goals published by the United Nations deal with the issue of water poisoning, namely clean water and sanitation and life below water (6 and 14 goals, respectively). Moreover, the World Health Organization (WHO) has stated that more than 10,000 people die every day due to diseases connected to the unavailability or contamination of clean drinking water [1].

The alteration of the natural water composition is predominantly caused by the increasing release of recalcitrant compounds in effluents and rivers. Indeed, next to an increment of the contamination caused by the most known Persistent Organic Pollutants

(POPs) [2], recently, the so called Contaminants of Emerging Concern (CECs) have appeared [3–5]. While the POPs include pesticides, herbicides, drugs, industrial chemicals and dyes, CECs are mostly new pollutants whose presence in effluents is related to the development of the welfare society. In this context, commercial dyes constitute one of the largest groups among the water pollutants, representing a growing environmental danger; they are widely used in textile, paper, rubber, plastic and cosmetic manufacturing plants, thus constituting a hazardous threat for the aquatic milieu and the dependent life on Earth. It has been estimated that up to 20% of the total world dye production is released into aquifers and waterways, so the discharge of those coloured wastewaters in the environment is a considerable source of non-aesthetic pollution and eutrophication and can originate dangerous by-products in the aqueous environment [6,7].

Generally, different physical and chemical processes such as precipitation by activated carbons, air stripping, coagulation, reverse osmosis, ion exchange on synthetic adsorbent resins and membrane nanofiltration have been adopted for the abatement of both POPs and CECs [8–11]. However, these technologies are very expensive and just transfer the contaminant compounds to another phase without effectively destroying them and thus cause secondary pollution [12]. In contrast to the traditional non-destructive procedures, a new highly efficient and promising approach, known as Advanced Oxidation Processes (AOPs), have been developed to treat wastewaters. AOPs involve many different technologies, such as Fenton oxidation and ozonisation under UV irradiation processes, characterized by the common use of generated hydroxyl radicals [7,8,13–17]. The hydroxyl ($^{\bullet}$OH) radical is a powerful and non-selective oxidant species, capable of degrading complex molecular structures [18,19]. Among AOPs, low-cost heterogeneous photocatalysis based on transition metal oxide semiconductor nanomaterials have arisen as one of the emerging destructive technologies. The key aspect of this approach is the inherent destructive nature of the photocatalyst matrix that doesn't involve mass transfer, it can be carried out under ambient conditions and leads to complete mineralization of organic carbon-containing compounds into water and CO_2 [20–23]. Undoubtedly, the great advantage of the heterogeneous photocatalysis derives from the possibility of utilizing naturally available and renewable solar energy for photochemical waste remediation. Throughout this process, highly oxidizing $^{\bullet}$OH radicals are produced following the photoexcitation of the semiconducting materials and the formation of electron-hole charge carriers. In details, once the photon energy, equal or larger the material band gap, is absorbed by the semiconducting matrix, the photoexcitation of the electrons from the valence band (VB) to the conduction band (CB) occurs; simultaneously, the photoinduction of holes in the VB takes place. When the photoinduced charge carriers reach the surface they can give rise to reductive and oxidative redox reactions: the electrons in the CB can be scavenged by molecular oxygen generating the superoxide radical species $^{\bullet}O_2^-$ that can be converted into reactive peroxide species, thus contributing to the molecular structure disruption of the water pollutant. On the other hand, the holes can oxidize a water molecule or a OH group at the surface to $^{\bullet}$OH radicals, that, as mentioned, are the most oxidant non-selective species that can bring about the complete mineralization of the hazardous compound [24–28].

Among all the transition metal oxide semiconductors tested for the photocatalytic purification of wastewaters, ZnO has certainly received great attention (second only to TiO_2) [29–40]. Moreover, some insulating materials, such as ZrO_2, have also been considered for photocatalytic applications [41–44]. However, despite the striking promising power of the photocatalytic approach for the abatement of harmful pollutants in water, many drawbacks exist preventing its implementation on a larger scale. The major shortcomings deal with the band gap extension, the rapid recombination of photogenerated charge carriers and the photocorrosion susceptibility. Especially in what concerns the band gap size, ZnO can only absorb in the UV range, with the absorption edge peaking around 380 nm, while ZrO_2, being an insulator, can absorb in the ultrahigh UV range, at almost 250 nm. In this regard, the UV radiation on the Earth surface accounts for less than the 5% of the total solar irradiation, too little to efficiently photo-activate these materials. On the

other hand, the visible contribution of the solar spectrum amounts to almost 48%, making this photon energy source more suitable to be employed to photoactivate transition metal oxide photocatalysts [45].

Different strategies have been developed to enhance the photocatalysts' visible photons absorption efficiency such as anion and cation doping [46–49], unsaturation of heterojunctions [50–54] and surface deposition [55–57]. Despite the great progress reached during the last years in the improvement of the photocatalytic ability by ZnO and also ZrO_2, a fully satisfying photodegradation efficiency able to supplant the mechanical physical and chemical technologies remains undeveloped.

In the last two decades research has focused its attention on doping with rare earth (RE) elements. The first papers dealing with lanthanide-doped transition metal oxide semiconductors described the doping of titanium dioxide with La, Ce and Yb for the photo-oxidation of acetone in air under UV irradiation [58]. This study paved the way for the investigation of Ln-doped semiconductors for photodegradation applications using UV and purely visible irradiation regarding the removal of POPs and CECs from wastewaters [59–65].

The lanthanide series in the periodic table spans from atomic number 57 (La) to 71 (Lu), including scandium and yttrium, thus collectively consisting of 17 elements. Most of them exhibit a $[Xe]6s^2 4f^n$ electronic configuration with n ranging from 0 to 14. The peculiarity of lanthanides arises from the shielding effect produced by the filled 5p65s2 sub-shell on the 4f orbitals, in such a way that allows intra f-f and f-d electronic transitions ranging from the UV to the visible spectral region, then giving rise to their fascinating and peculiar luminescence properties [66,67]. The electronic shielding of the 4f orbitals provided by the exterior orbitals guarantees a certain insensitiveness to the surrounding atomic environment, meaning almost no perturbations of these transitions. Depending on the lanthanide ion considered, different narrow transitions are feasible, establishing them as a unique chemical entity profitable for the enhancement of photocatalytic processes under visible irradiation. In this regard, the separated energy levels in Ln^{3+} ions can absorb near infrared photons and can afterwards release a photon with higher energy in the visible or UV range in the so called up-conversion process [68]. Practically, during the anti-Stokes absorption two or more near-infrared photons are absorbed subsequently by the rare-earth ion and a higher energy light quantum can be emitted. A great portion of the research in this field has considered the possibility of the employing the up-conversion process of lanthanides in order to utilize a higher portion of the solar spectrum for the conversion of visible wavelengths into UV light that can be absorbed by wide band gap transition metal oxide semiconducting matrixes. Moreover, lanthanide species are renowned to behave as strong Lewis acid, thus forming complexes with various Lewis bases, such as amines, aldehydes, alcohols, and thiols; when integrated in the semiconductor matrix, they can provide a means for the absorption of pollutants on the material surface, increasing its activity. Additionally, being strong Lewis acids, they can also favour the adsorption of oxygen, a vital species as electron scavenger at the material surface and successively for the production of peroxide species that can effectively contribute to the contaminant destruction [61,64,69].

In this mini-review we have focused our attention on the wide band gap transition metal oxides ZnO and ZrO_2 and their modifications when doped with cerium, europium and erbium, respectively. The selection of the lanthanide elements ranges from the beginning to the end of the lanthanide series, with the aim of describing the peculiarities resultingg from the different filling of the 4f orbitals. Previously published papers on this topic highlighted the improved photodegradation ability of the rare-earth doped oxides with respect to the bare materials, the stabilization of a particular crystallographic phase, the effect on the material band gaps and finally, in some cases, also the origin of so-called Visible Light Active systems (VLAs). Especially in the case of ZrO_2, a third-generation photoactive material based on the engineering and sensitization to visible light of high band gap oxides has seemed to be emerged. Indeed, as theorized by Serpone and Emilie, a

wide band gap semiconductor (hence with excellent flat band potentials) containing extra electronic levels in the middle of the forbidden gap can allow the transition of the electrons from the VB to the CB with a double excitation, employing the intragap states and thus reducing the energy for the transition that can effectively falls in the visible region: [69,70] this was verified for the Ce-doped ZrO_2 system [71–73].

Despite the great interest connected with the impressive improvement in the photocatalytic behaviours of the Ln-doped oxide materials, a detailed connections regarding the role of the lanthanide elements inside the inorganic host with the recorded photoactivity often lacks. In this work, we will try to give a complete and comprehensive overview concerning the structural, optical and electronic rule of the lanthanides elements within the selected oxide matrixes, highlighting their involvement in the working mechanism of light harvesting and charge carriers separation, as it comes out from the analysed literature. Our aim is pay the way for the production of increasingly efficient photoactive materials suitable for the complete mineralization of recalcitrant compounds in wastewaters by means the advantageous photocatalytic process.

For sake of brevity, we will not focus on the different parameters affecting the photocatalytic reactions, such as the photocatalyst loading, the pollutant concentration the light power or the solution pH; however, the manuscript is provided of several tables that will help the reader in the interpretation and understating of the considered complex systems. Finally, in Table 1 information about the structure, the production, the employment and the environmental risk of the encountered hazardous pollutants in the analysed literature are presented to contextualize the scenario: as it could be noted, most of them are organic dyes, in confirmation of their danger for the environment and the urgency to find a promising solution for their complete abatement.

Table 1. Molecular formula, weight and strcuture of the encountered pollutants. The absorption wavelenght, their production, employment and hazourdness are also reported.

Pollutant	Abbreviation	Molecular Formula	Molecular Weight (g/mol)	Molecular Structure	Absorption λ_{MAX} (nm)	Issues Generated
Rhodamine B	RhB	$C_{28}H_{31}ClN_2O_3$	479.02	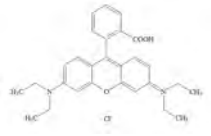	546	Industrial dye applied in paper printing, textile and leather industries. In addition, it is widely used as food colorant. It might develop gene-toxicity, mutagenicity, carcinogenicity.
Acetaminofene or Paracetamol	APAP or ACET	$C_8H_9NO_2$	151.163	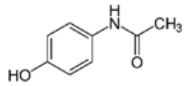	243	One of the most frequently consumed medicines in the world. It can be considered as emerging contaminants due to their toxicity and physiological effects even at low level.
Levofloxacin	LVFX	$C_{18}H_{20}FN_3O_4$	361.368	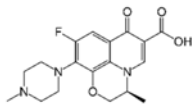	287	Drug uses for bacterial infections (i.e., pneumonia and diarrhoea). High toxicity for the marine flora. Its presence in aqueous environment can increase the antibiotic resistant of bacteria.
Nizatidine	NDMA	$C_{12}H_{21}N_5O_2S_2$	331.46	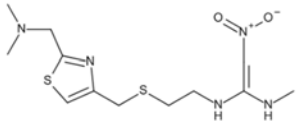	314	Used for gastrointestinal disorders. It is accused to be carcinogenic.
Methyl green dye	MG	$C_{27}H_{35}Cl_2N_3$	458.47	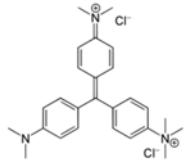	625	It is widely utilized to change solution colour in biology and medicine while serving as a photo-chromophore for exciting coagulated films. It is supposed to be toxic in water.

Table 1. *Cont.*

Pollutant	Abbreviation	Molecular Formula	Molecular Weight (g/mol)	Molecular Structure	Absorption λ_{MAX} (nm)	Issues Generated
Methyl Blue dye	MB	$C_{37}H_{27}N_3Na_2O_9S_3$	799.814	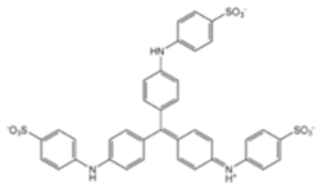	664	Employed for used for biological staining as well as colouring paper, hair, cottons and wools. In addition, MB injection is used in the treatment of urinary tract infections. Accumulation of MB in wastewater has adverse health effects such as difficulties in breathing, vomiting, eye burns, diarrhoea and nausea.
Methyl Orange dye	MO	$C_{14}H_{14}N_3NaO_3S$	327.34	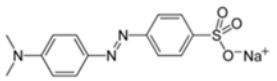	464	MO is known to be a pH indicator and as a dye in industry. It might cause respiratory tract irritation, nausea, vomiting, diarrhoea and central nervous system effects when ingested.
Bisphenol A	BPA	$C_{15}H_{16}O_2$	228.3	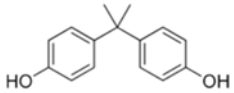	214	This compound is found in polycarbonate plastics and epoxy resins: often used in containers that store food and beverages. It exposure was associated with pregnancy loss, endometriosis, and endometrial hyperplasia.
Nonylphenol	NP	$C_{15}H_{24}O$	220.35	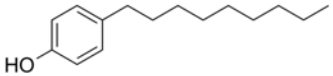	-	It is used as pesticide, plasticizer or solvent. It causes cause cancerous tumours and birth defects.
Acesulfame K	ACE	$C_4H_4KNO_4S$	201.242	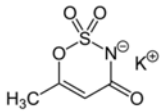	226	Widely employed as artificial sweetener. It is accused of causing cancer. The effect of CBZ on aquatic life, such as bacteria, algae, and fish, has been evaluated.

Table 1. *Cont.*

Pollutant	Abbreviation	Molecular Formula	Molecular Weight (g/mol)	Molecular Structure	Absorption λ_{MAX} (nm)	Issues Generated
Carbamazepine	CBZ	$C_{15}H_{12}N_2O$	236.269	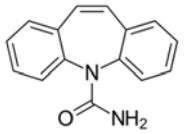	284	It is an antiepileptic drug widely used to treat seizure disorders, trigeminal neuralgia and bipolar disorder. The effect of CBZ on aquatic life, such as bacteria, algae, and fish, has been evaluated to cause cellular toxicity, apoptosis, geno-toxicity, and sexual disturbances in humans.
Sulfamethoxazole	SMX	$C_{10}H_{11}N_3O_3S$	253.279	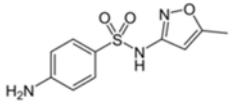	460	It is a is a bacteriostatic antibiotic. is useful for the treatment of a variety of bacterial infections, including those of the urinary, respiratory, and gastrointestinal tracts. Highly toxic for aqueous environment.
Atenolol	ATL	$C_{14}H_{22}N_2O_3$	266.34	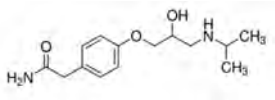	224	It's used to treat high blood pressure and irregular heartbeats. It might be dangerous for water fauna and flora.
Diclofenac	DCF	$C_{14}H_{11}Cl_2NO_2$	296.148	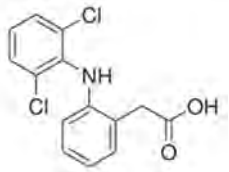	276	It is a non-steroidal anti-inflammatory drug. It is also used as antirheumatic and antianalgesic. It is believed to be a serious threat to vultures, aquatic animals, plants and mammals. Diclofenac can affect the development, growth and immune system.
Caffeine	CAF	$C_8H_{10}N_4O_2$	194.19	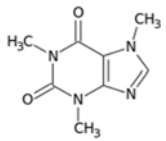	270	It is the constituent molecule of one of the most consumed drinks in the World. Given its still growing consumption its concentration in wastewater is forecasted to increase with unknown effect on various aqueous habitats.

Table 1. *Cont.*

Pollutant	Abbreviation	Molecular Formula	Molecular Weight (g/mol)	Molecular Structure	Absorption λ_{MAX} (nm)	Issues Generated
Ibuprofen	IBP	$C_{13}H_{18}O_2$	206.29	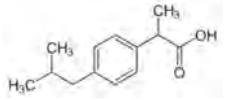	264/272	Active principle of many anti-inflammatory medicines. It is thought causing a potential threat to fish and water environment.
Phenol	-	C_6H_6O	94.11	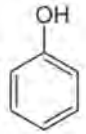	270/274	Widely used in household products and as intermediates for industrial synthesis. It has also antiseptic and disinfectant properties. Employed in the manufacture of plastics, explosives and drugs. Highly toxic to humans causing cancer and endocrine issues.
Reactive Black 5	RB5	$C_{26}H_{21}N_5Na_4O_{19}S_6$	991.8	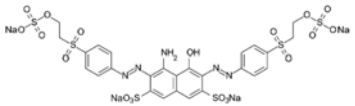	595	Employed in textile industries for cottons, viscose, wool and polyamide fabrics dyeing. It may cause allergy, asthma symptoms or breathing difficulties.
Acid Red azo dye	AR88	$C_{20}H_{13}N_2NaO_4S$	400.3	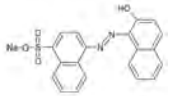	506	Widely employed in textile industry constituting 60–70% of the total dye production. It can be toxic, carcinogenic and mutagenic.
Cyanide	CN	CN^-	26.02		590	Widely used by electroplating and metal finishing units. It is well known for its poisoning effect.
Red-23 dye	DR-23	$C_{35}H_{25}N_7Na_2O_{10}S_2$	813.72	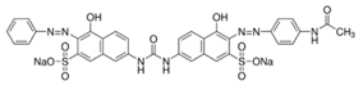	512	Mainly used in cosmetics and as pigments in textile industry; other sectors include pest control products, drugs, and natural health products. Thought to be toxic, carcinogenic and mutagenic.

Table 1. *Cont.*

Pollutant	Abbreviation	Molecular Formula	Molecular Weight (g/mol)	Molecular Structure	Absorption λ_{MAX} (nm)	Issues Generated
Crystal violet	CV	$C_{25}N_3H_{30}Cl$	407.979	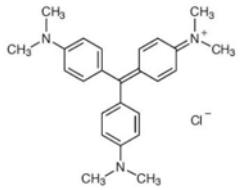	588	Used to dye paper and as a component of navy blue and black inks for printing, ball-point pens, and inkjet printers. It could pollute the animal feed and then the human food with still completely known effects.
Diatrizoate	DTZ	$C_{11}H_9I_3N_2O_4$	613.916	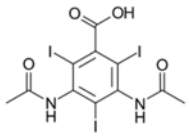	244	It is employed as a medical diagnostic agent for imaging blood vessels and organs (iodinated X ray contrast agent). It may have neph-rotoxic effects in animals and humans.
Iopamidol	IOPA	$C_{17}H_{22}I_3N_3O_8$	777.08	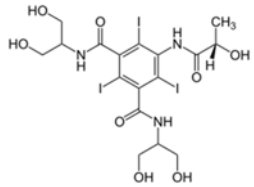	243	It is employed as a medical diagnostic agent for imaging blood vessels and organs (iodinated X ray contrast agent). It may have neph-rotoxic effects in animals and humans.
Iopromide	IOPRE	$C_{18}H_{24}I_3N_3O_8$	791.112	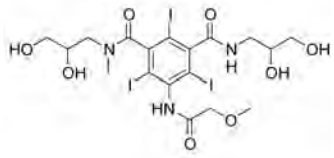	254	It is employed as a medical diagnostic agent for imaging blood vessels and organs (iodinated X ray contrast agent). It may have neph-rotoxic effects in animals and humans.

Table 1. *Cont.*

Pollutant	Abbreviation	Molecular Formula	Molecular Weight (g/mol)	Molecular Structure	Absorption λ_{MAX} (nm)	Issues Generated
Acid Yellow 29	AY-29	$C_{16}H_{10}N_4Na_2O_7S_2$	480.38	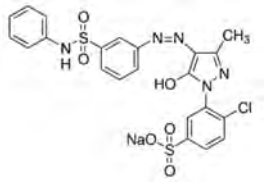	406	Employed in a wide variety of applications such as in pharmaceutical, personal care products and food additive. It is suspected causing deficiencies of zinc and tumours especially in women.
Coomassie Brilliant Blue G250	G250	$C_{47}H_{50}N_3O_7S_2+$	833.048	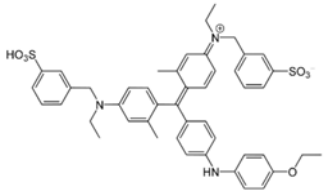	584	It is commonly used as an analyte specially to determine protein concentration; moreover, it is largely employment in various forensic science tests. It doesn't exist any indication about its toxicity or potential environmental issues.
Acid Green 25	AG-25	$C_{20}H_{13}N_2NaO_5S$	416.38	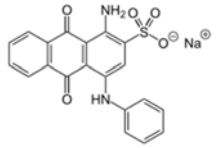	640	Employment as a colouring agent in cosmetic products, with particular development in hairs treatment. Any particular toxic effect is associated with this dye.
Malachite Green	MCG	$C_{23}H_{25}ClN_2$	364.911	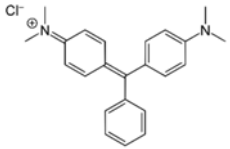	624	Mainly used as dye and pigment. Other employments involve staining biological specimens and the control of fungal and protozoan infections in fish. It is accused to generate genotoxic carcinogen at least in fishes.

Table 1. *Cont.*

Pollutant	Abbreviation	Molecular Formula	Molecular Weight (g/mol)	Molecular Structure	Absorption λ_{MAX} (nm)	Issues Generated
Humic Acid	HA	$C_9H_9NO_6$	227.17	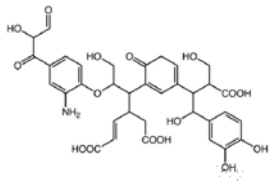	254	It is thought to be cause of cytotoxicity. Auto-immune diseases such as multiple sclerosis, lupus and rheumatoid arthritis might be emphasized by HA.
Congo Red	CR	$C_{32}H_{22}N_6Na_2O_6S_2$	696.665	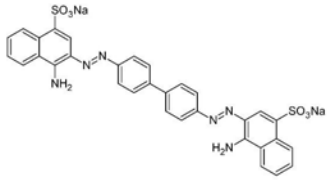	500	Dye employed in industry since its great resistance to washing and light. It is used in histology to stain tissues for microscopic examination, and to serve as an acid-base indicator. It has been predicted as potential genotoxic and carcinogenic chemical.
2-Mercaptobenzothiazole	MBT	$C_7H_5NS_2$	167.25	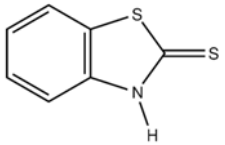	325	It is principally used as a reactant in the manufacture of rubber products, but is also used as a corrosion inhibitor in oils, greases, cooling fluids and as stabilizer for polyether polymers. It may cause an allergic skin reaction. It is very toxic to aquatic life with long-lasting effects.
Glyphosate	Gp	$C_3H_8NO_5P$	169.07	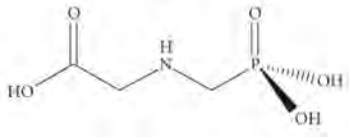	265	It is widely employed in agriculture as powerful herbicides for infest plants. Since 2005 it has been inserted in the list of substances accused of causing cancer in humans.

Table 1. *Cont.*

Pollutant	Abbreviation	Molecular Formula	Molecular Weight (g/mol)	Molecular Structure	Absorption λ_{MAX} (nm)	Issues Generated
Imidacloprid	IMCD	$C_9H_{10}ClN_5O_2$	255.70	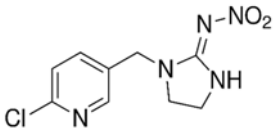	268	It is a widespread insecticide. It has important repercussions on aquatic fauna, especially for algae and crustaceans. It seems to be one of the main responsible for the die-off of bees
Quinalphos	QP	$C_{12}H_{15}N_2O_3PS$	298.30	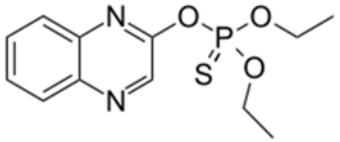	235	It is employed as herbicides in developing countries, especially India, in different crops such as wheat, rice and coffee. Its used is not approved in Europe since it seems to be connected to several blood diseases.
Deoxynivalenol	DON	$C_{15}H_{20}O6$	296.32	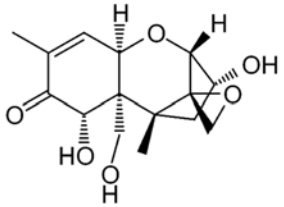	218	It is high-toxicity secondary metabolite produced by *Fusarium graminearum* , one of the most common mycotoxins in grains, foods and feeds. It has various toxic effects on the metabolism of humans and animals, such as inhibition of protein synthesis and nucleic acids. It causes leukaemia and anaemia. It is considered a carcinogen.
2,4-Dichlorophenoxyacetic	2,4-D-acid	$C_8H_6Cl_2O_3$	221.04	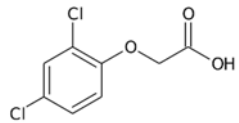	229	It is one of the first and most common herbicide employed in the world. It may cause fertility problems for men. It can also cause eye irritation. it is accused of causing cancer when exposure is high

Table 1. *Cont.*

Pollutant	Abbreviation	Molecular Formula	Molecular Weight (g/mol)	Molecular Structure	Absorption λ_{MAX} (nm)	Issues Generated
Reactive brilliant X-3B	X-3B	$C_{19}H_{10}Cl_2N_6Na_2O_7S_2$	615.3	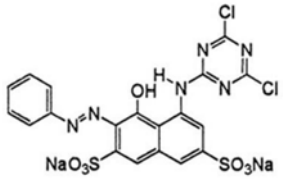	270	Water soluble azo dye used in industry as red colorant. It may deliver harmful aromatic amines considered carcinogenic.
Rhodamine 6G	Rh6G	$C_{28}H_{31}N_2O_3Cl$	479.02	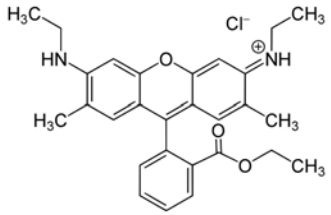	526	Lipophilic dye used for natural and synthetic fibers and in biomedical research. It causes long term adverse effects in the aquatic environment and can be harmful for human health after long term exposure.
Eriochrome black T	EBT	$C_{20}H_{12}N_3O_7SNa$	461.38	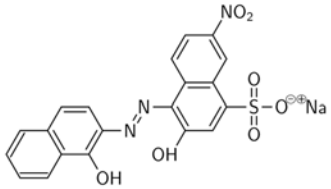	580	Azo dye widely used for silk, wool, nylon dyeing and in laboratories as a complexometric titrant agent. It is toxic and carcinogenic.

Table 1. *Cont.*

Pollutant	Abbreviation	Molecular Formula	Molecular Weight (g/mol)	Molecular Structure	Absorption λ_{MAX} (nm)	Issues Generated
Acid Red 17	AR17	$C_{20}H_{12}N_2Na_2O_7S_2$	502.4	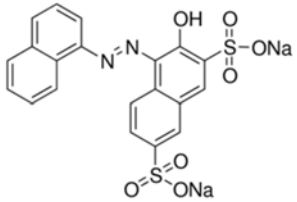	510	Anionic azo dye used in the textile industry and food industries like cereals, candies, dairy products, jellies, ice creams and powdered juices.
Indigo Carmine	IC	$C_{16}H_8N_2Na_2O_8S_2$	466.36	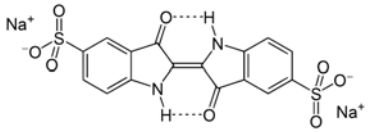	610	Vat dye mainly used in the textile industry for the dyeing of polyester fibers and denim, in food industry, cosmetics industries, as a diagnostic aid, as a redox indicator in analytical chemistry, and as a microscopic stain in biology. It is a highly toxic indigoid dye and might cause skin and eye irritations to human beings. It can also cause permanent injury to cornea and conjunctiva, is carcinogenic and can lead to reproductive, developmental, neuro and acute toxicity.
Acetylsalicylic Acid	ASA	$C_9H_8O_4$	180.16	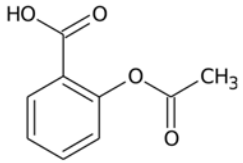	276	Aspirin, also known as acetylsalicylic acid (ASA), is a non-steroidal anti-inflammatory drug (NSAID) of the salicylate family. Several studies have reported the presence of this pharmaceutical compound in lakes, rivers, and freshwater environments.

Table 1. *Cont.*

Pollutant	Abbreviation	Molecular Formula	Molecular Weight (g/mol)	Molecular Structure	Absorption λ_{MAX} (nm)	Issues Generated
4-nitrophenol	4-NP	$C_6H_5NO_3$	139.11	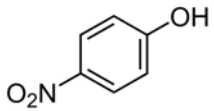	313	Nitrophenols are major contaminants in agricultural and industrial wastewater due to their water solubility. The US Environmental Protection Agency has classified nitrophenols as critical contaminants since they can cause organ damage, blood disorder and impairment in the central nervous system.
2-chlorophenol	2-CP	C_6H_5ClO	128.56	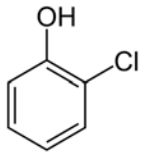	275	It has been named as priority pollutants by the US EPA. The stability of the C-Cl bond is responsible for its toxicity and persistence in the biological environment. It is employed as intermediate in the production of higher chlorinated phenols or phenoxy herbicides. It can be introduced into the environment through discharges from paper mills as by-products of chlorine-based bleaching, as a result of disinfection of sewage and industrial wastewater with chlorine and from slow microbial breakdown of herbicides during post-application period. The compound is also used as a solvent for extracting sulfur and nitrogen compounds from coal.

Table 1. *Cont.*

Pollutant	Abbreviation	Molecular Formula	Molecular Weight (g/mol)	Molecular Structure	Absorption λ_{MAX} (nm)	Issues Generated
Orange G	OG	$C_{16}H_{10}N_2Na_2O_7S_2$	452.37	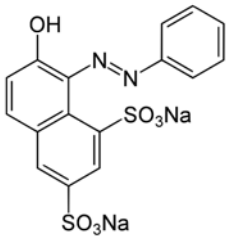	478	Azo dye used in textile and paper industries. It is resistant to aerobic degradation and can be reduced to potentially carcinogenic aromatic amines under anaerobic conditions or in vivo. Its release into the environment is a considerable source of non-aesthetic pollution and eutrophication which can produce dangerous by-products through oxidation, hydrolysis, or other chemical reactions taking place in the wastewater.

2. Cerium

Among all the rare-earth ions used as a dopant in semiconducting matrices aimed at enhancing the visible light absorption and photoactivity in the degradation of harmful pollutants in wastewater, cerium is undoubtedly the most explored. This is probably due to the fact that it is the most abundant of the lanthanides and also that the redox properties of its oxidized form CeO_2 are employed in various other branches of catalysis. Further, the easy transition between the oxidized and reduced states depending on the reaction conditions has been crucial in the dissemination of this oxide in the catalytic field [74,75]. In particular, its oxygen storage capability makes ceria an appropriate catalyst for different catalysed reactions such as steam reforming [76], oxidation reactions [77,78], and water-gas shift reactions [79].

Despite its wide use in catalysis, its direct application in photocatalysis is limited by a band gap energy value of almost 6 eV [80], typical of an insulating material and thus too large for charge carrier separation promoted by visible photons. However, as will be reported hereafter, the presence of CeO_2 with the considered oxides can improve the charge carrier separation reducing electron-hole pair recombination.

Considering the [Xe] $4f^1$ $5d^1$ $6s^2$ electronic configuration of cerium, the oxidized Ce^{4+} state is characterized by empty 4f orbitals, while in the Ce^{3+} reduced state it hosts one electron: the predicted standard redox potentials for the Ce^{4+}/Ce^{3+} transition is about 1.76 V.

Differently from other lanthanides, it has been reported that the role of cerium inside ZnO and ZrO_2 matrixes greatly changes in going from one oxide to the other. In general, the promotion of the photocatalytic activity is reached via a considerable modification of the structural, optical and electronic properties of the starting material, in which both electron-hole pair separation and the absorption of visible wavelengths is improved.

2.1. Ce-Doped ZnO

Among the oxides modified with rare earth elements with the aim of improving their photodegradation behaviour towards wastewater, the most investigated results correspond to Ce-doped ZnO. However, despite the high number of publications in which the photodegradation capability of ZnO is greatly improved by the presence of Ce, also upon visible irradiation, different schools of thought exist concerning the effective role of cerium inside ZnO. From a structural point of view, the most common explanation consists in the description of a classical doped compound, in which Ce^{4+} substitutes Zn^{2+} in the wurtzite structure and consequently causes a charge decompensation; this trend doesn't seem to be affected by the type of synthesis procedure employed in the preparation of the material. Indeed, from numerous manuscripts it emerges that both hydrothermal [81–84], precipitation [85–89], microwave [90–92], ball milling [93] and sonochemical [94–96] synthetic routes result in the detection of the wurtzitic hexagonal phase typical of bare ZnO. At this regard, Elias et al. [90,91] and Ha et al. [84] have stated that the insertion of cerium atoms inside the crystallographic environment of ZnO can reached up to 5 mole% of the rare-earth element. As suggested by DFT calculations, the insertion of Ce into the ZnO lattice is energetically stable, affecting the crystal size, lattice strain, bond length and lattice parameters with respect to bare ZnO [97]. In addition to the alteration of the lattice parameters, the insertion of Ce^{4+} would also increase the number of intrinsic defects in zinc oxide due to charge compensation, especially generating oxygen vacancies (V_O) [98]. As described in the following paragraphs, the growth of V_O concept is one of the referred interpretations of the improved photocatalytic activity in Ce-doped ZnO. In several cases, the claimed successful doping procedure was evaluated by means XRD analysis, where the modification in the bulk structure of ZnO by Ce insertion is monitored by the shift at lower 2θ angles of the reflections in the XRD pattern between the doped and undoped materials [84,95,98] as reported in Figure 1A. Moreover, the different structural analyses for the determination of the lattice parameters are mainly performed via the Debye-Scherrer formula and Rietveld refinement [99,100]. A general trend emerging from the literature

data is that the substitution of Zn^{2+} sites with Ce^{4+} ions expands the ZnO unit cell resulting in a shift in the diffraction pattern, as disclosed by Wang et al. [86,95].

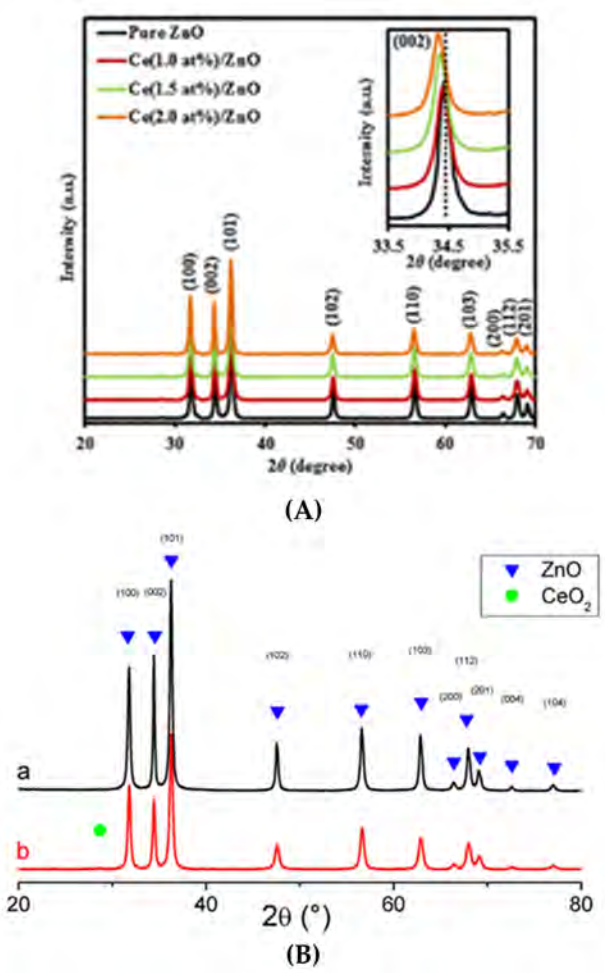

Figure 1. (**A**) XRD patterns of pure ZnO and Ce-ZnO with different Ce doping contents. The inset is the magnified region of the (0 0 2) reflection. Reprinted with permission from [86] Copyright Elsevier (2015). (**B**) XRD patterns of (a) ZnO and (b) 1%Ce-ZnO. Reprinted with permission from [101] Copyright ACS (2018).

On the other hand, a defined structural portrait of the modified material is complicated by the fact that same synthetic methods with similar dopant percentages lead to the formation of a biphasic solid constituted by means of CeO_2-ZnO interfaces generating a heterojunction system [101–107], appreciable in Figure 1B. In this way it results challenging to identify a synthesis or a specific cerium percentage that could drive the system toward a doped material respect to a heterojunction one and vice versa (see Table 2). Still, in very few cases the formation of the Ce_2O_3 phase instead CeO_2 has been reported, as in the case of Kaneva et al. [93], where it was identified by TEM analysis. Indeed, TEM analysis coupled with EDX maps has been pivotal for the identification of the further phases related to cerium oxide. An exemplary case is reported in Figure 2, where Paganini et al. [108] were able to distinguish the CeO_2 phase anchored on a ZnO surface confirming the XRD analysis results; in addition, no contamination by cerium atoms was detected inside or at the interface with the ZnO matrix. Also Caregnato et al. were able to identify the presence of CeO_2 decorating ZnO nanoparticles via TEM analysis and Raman spectroscopy [109].

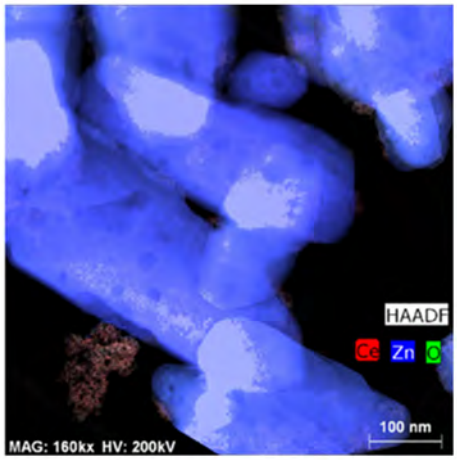

Figure 2. EDX atomic maps of Ce (red), Zn (blue) and O (green) for Ce-doped ZnO sample. Reprinted with permission of Ref. [108] Copyright Chemistry Europe 2016.

Nevertheless, the crystallographic depiction of the designed system in terms of a biphasic solid or of a doped one greatly affects the interpretation of the final material, especially in the explanation of the enhanced photodegradation ability respect to bare ZnO. For this reason, the determination of the crystal structure and of the phases present in the final material is a first step of paramount importance in the evaluation of the charge carrier dynamics induced by photon absorption. In addition to the most reported doped systems or CeO_2-ZnO biphasic solids, the formation of the $Ce_{1-x}Zn_xO_2$ solid solution has been also suggested by Bazta et al. [110]. Definitely, in light of the considered data, the description of a biphasic solid rather than a doped system or a solid solution seems being more feasible considering both the different crystal environments in which the Zn^{2+} (tetrahedral) and Ce^{4+} (octahedral) atoms prefer to crystallize (hexagonal and cubic structures, respectively) and the difference in the ionic radii for Zn^{2+} and Ce^{4+} (0.74 Å vs. 0.97 Å, respectively); even so, a mutual contamination of the two oxides at the interfaces cannot be completely excluded. Still, considering the Hume-Rothery rule, the solid solution in Ce-doped ZnO is not likely to occur since the difference in the ionic radii between the host and the guest is larger than 15% [59,88,99].

Generally, both in the case of the hypothetical insertion of Ce inside the ZnO lattice and in the instauration of CeO_2-ZnO interfaces, a reduced intensity and a broadening of the XRD reflections is often recorded, indicating that the presence of Ce ions in the form of dopant or as ceria causes a reduction of the material's crystallinity. This phenomenon also implies a decrease of the crystallite size with a significance increase in the exposed surface area [59,84]. Indeed, in the case of the biphasic solid the presence of CeO_2 inhibits the further growth of the ZnO nanoparticles reducing their agglomeration during the material precipitation; in a similar way, in a doped system, Ce ions would limit the growth of the ZnO matrix due to the creation of inhomogeneity in the wurtzitic crystal lattice or due to their stabilization in grain boundaries and dislocations [100].

Passing to the optical features of the Ce-doped ZnO system, it is possible to assert that the introduction of Ce inside the ZnO lattice or the establishment of the CeO_2-ZnO interface often induces a slight red-shift respect to the pristine ZnO absorption, as depicted in Figure 3 and Table 2, where very different values for the energy gaps of the designed materials are observed. For what concerns the different energy gap values reported in the literature, various interpretations of the role of cerium related to the alteration of the optical properties of ZnO have been considered. The most popular assumption is that the inclusion of Ce in the lattice sites of ZnO can generate discrete energy levels between the VB and the CB: the presence of such localized electronic energy states is suggested by the strengthened visible photon absorption. In particular, the empty localized 4f orbitals of Ce^{4+} below the conduction band edge would guarantee a narrow charge transfer between the 4f

energy level and the conduction/valence bands of ZnO, with the consequent improved photodegradation activity [88,89,95,96,111–113]. Within this description, the presence of cerium is also believed to reduce the electron-hole pair recombination, where the easy Ce^{3+}/Ce^{4+} conversion should be the key step, with Ce^{4+} acting as an electron scavenger and Ce^{3+} as an electron donor. Definitely, the dense populated defective energetic states at the bottom of the ZnO conduction band would increase the density of free electrons and thus provoke the moving up of the Fermi level resulting in a n-type doping. However, as emerged already from structural analysis, the presence of cerium during the preparation of ZnO-modified materials can also give rise to a biphasic CeO_2-ZnO heterojunction. Also in this case an improved visible light absorption was registered respect to ZnO (Figure 3B) and associated to the enhanced catalytic degradation of pollutants ability; however, its origin is different respect the one suggested for Ce hosted in a lattice site. Indeed, although the insulating behaviour of CeO_2 with a band gap of 6 eV, the presence of 4f orbitals at less than 3 eV from the VB edge allows the electronic transition, promoted by visible photons [81,102,107,114]. Thus, the additional absorption centred around 450 nm would arise from the electronic transition from the valence band to the empty discrete 4f states of Ce^{4+}. Nevertheless, some authors start from the assumption that the energy gap of CeO_2 is 3 eV and their suggestion for the visible absorption evidence would be due to the charge transfer from Zn conduction band to CeO_2 conduction band [114,115]. Nevertheless, Kumar et al. reported a blue-shift when cerium was inserted into ZnO: in this case, the increase of the band gap value is referred to the small size of the Ce-doped ZnO nanoparticles as consequence of the presence of cerium [100].

Certainly, it is extremely difficult to draw a unified conclusion about the influence of cerium presence concerning the modification of the band gap; in general, it doesn't seem to be affected by the preparation method. Connected to this uncertainty aspect, in the following we will show the different suggested working mechanisms for the Ce-doped ZnO material, critically discussing the various options proposed in the literature.

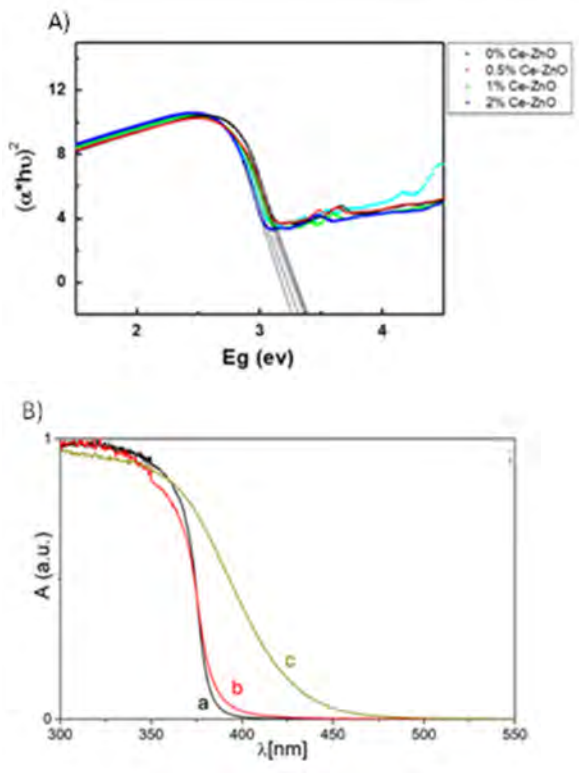

Figure 3. (**A**): UV–vis of the samples ZnO and Ce-doped ZnO. Reprinted with permission from [83] Copyright Elsevier (2015). (**B**): Absorbance (Kubelka–Munk transformed diffuse reflectance) spectra of (a) ZnO, (b) CZ1, and CeO_2. Reprinted with permission from [101] Copyright ACS (2018).

As summarized in Table 2, Ce-modified ZnO has been used for the degradation of a large variety of classical and emerging pollutants in wastewater, including dyes such as methylene blue [84,89–91,95,96,107,110,116–119] and rhodamine [88,103,113,120], pharmaceuticals such as ibuprofen and paracetamol [121] and industrial contaminants like bisphenol-A [83,85,87] and acesulfame-K [105]; moreover, the photodegradation of a class of medical diagnostic agents such as X ray contrast agents (ICM) has been also reported [108]. As often happens in manuscripts dealing with photocatalytic applications, the parameters affecting the final photocatalytic ability differ from one investigation to another, making the evaluation and the comparison of the performance of different materials really difficult. However, some guidelines regarding how the designed material works upon irradiation in the successful abatement of compounds in aqueous media can be extrapolated, in order to provide even more proficient photocatalysts, with particular attention to visible light absorption. In this regard, the most common explanation for the improved charge carrier separation induced by light absorption and the resulting increased photodegradation ability for Ce-modified ZnO deals with the role played by the 4f orbitals of Ce^{4+}. In particular, the cerium would act as the electronic mediator for the photoexcited electrons from the conduction band of ZnO, therefore reducing Ce^{4+} to Ce^{3+} [87,93,103,122]. Indeed, the Ce^{4+}/Ce^{3+} redox pair is supposed to live below the ZnO CB, thus facilitating the trapping of excited electrons from the VB upon irradiation as depicted in Figure 4A. Definitely, the cerium ions hosted in the ZnO lattice would speed up the photogenerated electrons inducing a delay in the electron-hole pairs recombination. Commonly, this occurrence is supposed to be experimentally demonstrated by means photoluminescence spectroscopy: [98,103] this arouses from the fact that a reduction of the band edge recombination signal for ZnO has been often recorded with the increase of cerium content. Still, the Ce^{4+} behaves as a stronger Lewis acid than O_2 and therefore it can scavenge the CB electrons rapidly in such a way to restrain from the recombination with the holes [59]. The modelling for the photodegradation mechanism of Ce-doped ZnO proceeds stating that the photoinduced Ce^{3+} species interacts with molecular oxygen leading to superoxide anion $O_2^{\bullet -}$ and Ce^{4+}; [81,120] within the reaction environment $O_2^{\bullet -}$ can be easily converted to $^{\bullet}OH$ species, thus contributing to the purification activity [123].

Table 2. Ce concentration, structure, morphology, band gap and reaction condition used for the degradation of various pollutants for different Ce-doped ZnO studies.

Synthetic Route	Ce Contempt	Structure and Morphology	E_{gap} (eV)	Irradiation Source (Power, W)	Pollutant Nature	Pollutant Concentration (mg/L)	Photocatalyst Concentration (g/L)	Best Degradation Efficiency	Ref.
Combustion	0.5–10 wt.%	Highly porous CeO_2-ZnO Nanopowders		Vis-light ($\lambda \geq$ 420 nm, 400 W)	RhB	15	1	3 wt.% Ce, 69% after 2 h	[102]
Hydrothermal	1–5%	Wurtzitic	1%: 3.15 3%: 3.17 5%: 3.16	UV-B (8 W)	APAP, LVFX and NDMA	5	1	1%Ce, 95% after 4 h for Acetaminophen and Levofloxacin	[81]
Milling of the precursor and calcination	1–7.5 wt.%	Biphasic CeO_2-ZnO Nanorods	1%: 3.25 2.5%: 3.27 5%: 3.29 7.5%:3.28	UV light (16 W)	MG	20	2	7.5 wt.% Ce, 100% after 30 min	[124]
Microwave	1–3 wt.%	Biphasic CeO_2-ZnO system for 3% Ce or $Ce_{1-x}Zn_xO_2$ solid solution	1%: 3.40 2%: 3.26 3%: 3.17	UV-vis	MB	10	0.08	2 wt.% Ce, 95% after 2 h	[110]
Hydrothermal	2 mol%	Wurtzitic	3.23	UV (λ = 254 nm, 30 W)	BPA	50	1	67% after 25 h	[82]
Hydrothermal	0.5–4 mol%	Wurtzitic	0.5%: 3.29 1%: 3.28 2%: 3.23 4%: 3.26	UV (λ = 254 nm, 30 W)	BPA NP	50	-	2 molar% Ce	[83]
Hydrothermal	0.5, 1 mol%	Biphasic CeO_2-ZnO system	3.27	Vis-light ($\lambda \geq$ 430 nm, 750 W)	ACE	20	-	1 molar% Ce, 60% after 90 min	[105]
Sol-gel	5 at%	Biphasic CeO_2-ZnO system	-	Vis-light ($\lambda \geq$ 575 nm)	CBZ	15	1	53% after 3 h	[109]
Sol-gel	2–7 wt.%	Biphasic CeO_2-ZnO mesoporous system	2%: 3.01 5%: 3.05 7%: 3.06	UV (λ = 360 nm, 20 W)	MO	30	0.5	2% wt.% Ce, 100% after 90 min	[105]
Precipitation	0.15, 0.2 mol%	Wurtzitic Nanorods	0.15%: 3.18 0.2%: 3.10	Vis-light	MO	10		0.2 molar% Ce, 100% after 80 min	[85]
Microwave	5 wt.%	Wurtzitic Nanotubes	3.26	UV (λ = 362 nm, 60 W)	MB	5	0.5	96.4% after 4 h	[90]

Table 2. *Cont.*

Synthetic Route	Ce Contempt	Structure and Morphology	E_{gap} (eV)	Irradiation Source (Power, W)	Pollutant Nature	Pollutant Concentration (mg/L)	Photocatalyst Concentration (g/L)	Best Degradation Efficiency	Ref.
Microwave	5 wt.%	Wurtzitic Thin film	1.92	Vis-light (200 W)	MB	5	-	76.7% after 4 h	[91]
Hydrothermal	1 mol%	-	-	UV-Vis (λ_{max} = 360 nm, 60 W)	CBZ, SMX, ATL, BPA, DCF, CAF, IBP	2	1	100% after 30 min for CBZ, BPA and DCF	[122]
Hydrothermal	0.1–5 mol%	Biphasic CeO_2-ZnO Nanorods	0.1%: 2.89 0.25%: 2.83 0.5%: 2.78 3%: 2.91 5%: 2.92	UV (250 W)	MB	6.4	0.4	0.5 molar% Ce, 100% after 90 min	[107]
Hydrothermal	1–5 mol%	Wurtzitic From Flower-like to Nanorods	1%: 3.256 3%: 3.256 5%: 3.250	Vis-light (UV filter, 250 W)	MB	7	1	3 molar% Ce, 100% after 90 min	[84]
Precipitation	1–2 mol%	Wurtzitic Nanospheres	1%: 3.20 1.5%: 3.15 2%: 3.13	Vis-light (UV filter, 55 W)	Phenol	20	1	3 molar% Ce, 100% after 90 min	[86]
Precipitation	0.1–0.5 mol%	Wurtzitic Hollow Nanospheres	-	UV-vis (500 W)	RhB, MO	10	0.4	0.3 molar% Ce, 99% after 90 and 30 min for MO and RhB, respectively	[87]
Milling	2 mol%	Wurtzitic Flower-like	-	UV	RB5	20	0.5	65% after 35 min	[93]
Chemical Bath deposition	1–20 mol%	Wurtzitic for 1% and 5%; Biphasic CeO_2-ZnO for 10% and 20% Nanorods	1%: 3.17 5%: 3.19 10%: 3.21 20%: 3.22	Vis light ($\lambda \geq 400$ nm, 50 W)	AR88	10	-	1 molar% Ce, 31% after 3.5 h	[113]
Sonochemical wet impregnation	2 mol%	Wurtzitic	3.08	UV (λ = 365 nm, 64 W)	CN	250	4	35% after 30 min	[94]
Precipitation	1–10 mol%	Wurtzitic for 1% and 5%; Biphasic CeO_2-ZnO for 10%	1%: 3.28 5%: 3.36 10%: 3.36	UV (125 W)	MO	10	1	5 molar% Ce, 97% after 3 h	[100]

Table 2. *Cont.*

Synthetic Route	Ce Contempt	Structure and Morphology	E_{gap} (eV)	Irradiation Source (Power, W)	Pollutant Nature	Pollutant Concentration (mg/L)	Photocatalyst Concentration (g/L)	Best Degradation Efficiency	Ref.
Precipitation	1.5–4 mol%	Biphasic CeO_2-ZnO	-	UV (125 W)	DR-23	40	0.5	3.5 molar% Ce, 100% after 100 min	[125]
Precipitation	1–4 mol%	Wurtzitic for 1% and 2%; Biphasic CeO_2-ZnO for 3% and 4%	-	UV (λ = 365 nm, 250 W)	MO	5	-	2 molar% Ce, 89.5% after 240 min	[126]
Hydrothermal	0.25–5 mol%	Wurtzitic for lower %; Biphasic CeO_2-ZnO for 3% and 5% 3D Microflowers	0.25%: 3.04 0.5%: 3.01 1%: 2.98 3%: 2.96 5%: 2.93	UV (175 W)	RhB	8	2	1 molar% Ce, 70% after 150 min	[112]
Sonochemical	2–8 mol%	Wurtzitic for 2% and 4%; Biphasic CeO_2-ZnO for 6% and 8%. Nanorods	2%: 3.35 4%: 3.33 6%: 3.32 8%: 3.31	Sun-light	CV	50	0.2	4 molar% Ce, 100% after 100 min	[127]
Hydrothermal	1 mol%	Biphasic CeO_2-ZnO Flower-like	3.27	UV (λ = 290–400 nm, 24 W)	DTZ, IOPA, IOPRE	20	1	100% after 30, 120 and 240 min for IOPA, IOPRE and DTZ, respectively	[108]
Microwave	3–12 mol%	Wurtzitic for 3%; Biphasic CeO_2-ZnO for 6%, 9% and 12%. Nanoflowers	3%: 3.12 6%: 3.10 9%: 3.08 12%: 3.03	UV (λ = 254 nm, 24 W)	MB	-	-	12 molar% Ce, 94% after 50 min	[116]
Combustion	1–5 mol%	Wurtzitic for 1%; Biphasic CeO_2-ZnO for 3%, 5%. Nanoflowers	-	UV (16 W)	MB	6.4	1.5	5 molar% Ce, 65% after 300 min	[117]
Precipitation	0.5–2.5 mol%	Wurtzitic	0.5%: 3.16 1%: 3.08 1.5%: 2.81 2%: 2.93 2.5%: 2.97	Vis light (500 W)	AY-29, G250 and AG-25	AY-29: 120 G250: 208 AG-25: 104	1	2 molar% Ce, 51.15%, 58% and 55% after 2 h for AY-29, G250 and AG-25, respectively	[88]

Table 2. *Cont.*

Synthetic Route	Ce Contempt	Structure and Morphology	E_{gap} (eV)	Irradiation Source (Power, W)	Pollutant Nature	Pollutant Concentration (mg/L)	Photocatalyst Concentration (g/L)	Best Degradation Efficiency	Ref.
Microwave	0.25–1.5 mol%	Biphasic CeO_2-ZnO	-	-	MB	-	0.8	1 molar% Ce, 100%, after 100 min	[118]
Refluxing	0.25–1 mol%	Wurtzitic	0.25%: 3.16 0.5%: 3.08 0.75%: 2.81 1%: 2.93	UV (125 W)	MB	8.8	0.4	0.5 molar% Ce, 100%, after 100 min	[89]
Ball milling	1–10 wt.%	Biphasic CeO_2-ZnO Nanorods-Nanowires	-	UV (λ = 365 nm, 125 W)	MB	2.5	8×10^{-3}	1 molar% Ce, 96.3%, after 80 min	[119]
Microwave	1 mol%	Wurtzitic Nanoflowers	2.5	Vis-light (λ_{max} = 490 nm, 250 W)	MCG	5	-	100% after 5 h	[92]
Precipitation	0.5–2 mol%	Wurtzitic for 0.5% and 1%; Biphasic CeO_2-ZnO 2%. Mesoporous Nanoflowers	0.5%: 3.12 1%: 3.08 2%: 3.11	Simulated sunlight (500 W)	RhB, Phenol	20	1	1 molar% Ce, 85.1% and 69.4% after 2 h for RhB and phenol, respectively	[128]
Solution	1–8 mol%	Wurtzitic Nanoflowers	1%: 3.09 3%: 3.07 5%: 3.04 8%: 3.02	UV (λ_{max} = 365 nm, 250 W)	MB	10	0.4	1 molar% Ce, 96.11% after 140 min	[95]
Sonochemical	3 mol%	Wurtzitic Nanoneedles	-	UV	MB	3.2	5	98% after 5 h	[96]

On the other hand, the photoinduced holes in the valence band of ZnO can get trapped on the material surface undergoing charge transfer with absorbed water molecules and surface bond hydroxide species to generate active •OH radicals, crucial agents for the complete mineralization of the contaminants [87,115,129]. A further suggestion about the role of cerium within the ZnO matrix is associated with an increase of the defectivity in the oxide, notably oxygen vacancy (V_O) and zinc vacancy (V_{Zn}). The further defectivity introduced by the presence of cerium would still contribute to the reduced charge carrier recombination and has been mainly detected via PL spectroscopy [85,86,114,118].

An alternative explanation concerning the working mechanism in the enhanced photocatalytic ability for ZnO modified with cerium involves the stabilization of Ce species at the surface rather than in the bulk of the material [113,121,122,128]. Once again, the reversible reduction/oxidation behaviour of the Ce^{3+}/Ce^{4+} redox couple would favour and guarantee the trapping of photoexcited electrons and the subsequent charge donation to the oxygen molecules, as reported in Figure 4B.

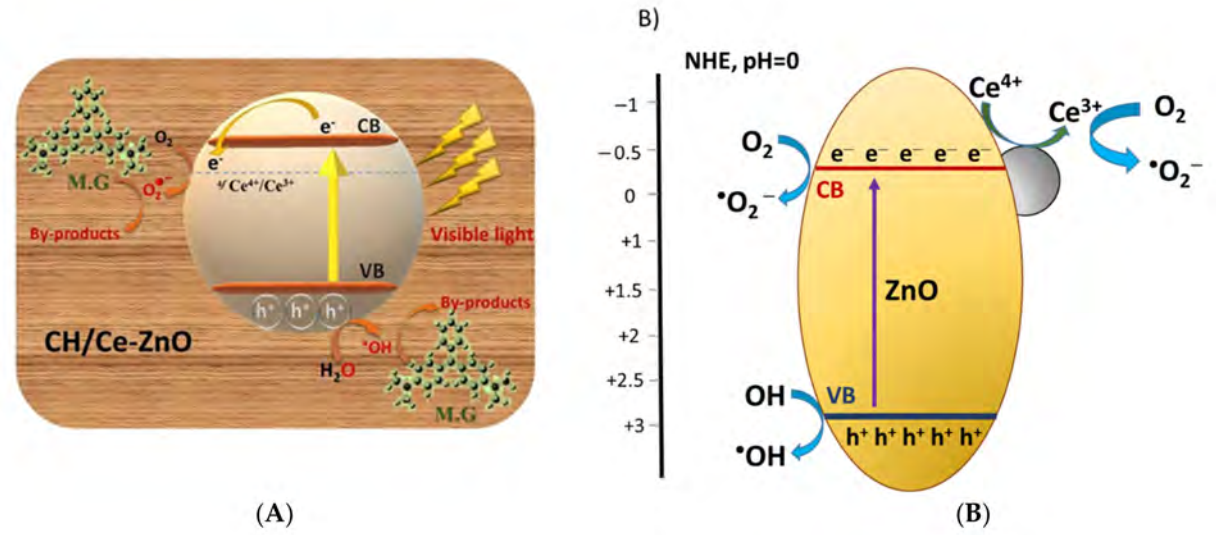

Figure 4. (**A**): Suggested photodegradation mechanism for the methyl green dye by the Ce-doped ZnO material supported on Chitosan (CH). Reprinted with permission from [92] Copyright Elsevier (2020). (**B**): Proposed mechanism for the production of Reactive Oxygen Species (ROS) by Ce stabilized at the ZnO surface.

The working mechanisms mentioned above doesn't appropriately explain all the experimental evidence collected in different analysed papers; inter alia, the frequent occurrence of the biphasic solid CeO_2-ZnO and a reliable reason for the improved photocatalytic activity under visible light. In particular, for this last aspect, not many suggestions have been put forth: indeed, the fact that the 4f orbitals could host photoexcited electrons from the ZnO VB retaining the electron-hole pairs recombination doesn't necessarily justify the visible photon absorption. In this respect, Cerrato et al. proposed a convincing working mechanism for the CeO_2-ZnO interface that presumably involves the proper establishment of a form arising from the synthesis of ZnO in the presence of Ce rather than an actual doped system. In their investigation they performed EPR measurements at 77 K with in situ irradiation both in vacuum and under gas atmospheres in order to monitor the charge carrier separation and their pathway in the bulk and at the surface of the material. It turns out that the main part of photoexcited of electrons are stabilized on CeO_2 oxide, specifically in the empty localized 4f orbital of Ce^{4+} that is reduced to Ce^{3+}, while the photoinduced holes remain free in the ZnO valence band [101]. Moreover, the DFT calculations highlighted a peculiar atomic arrangement at the interface of the two oxides that can reduce the band gap at the interface, becoming photoactive under visible irradiation and implying a heterojunction working mechanism, as displayed in Figure 5. Thus, as widely developed in this section, different experimental evidence justifies the occurrence of an

unstauration of the CeO_2-ZnO heterojunction rather than a real doping system, with the substitution of Zn^{2+} with Ce^{4+} in the ZnO network: the improved photocatalytic ability has therefore to be assigned to the improved charge carrier separation at the oxide interface, with stabilized holes in the ZnO and electrons in CeO_2. Moreover, a reduced material band gap is expected at the interface due to the peculiar atomic arrangement as suggested by theoretical calculations.

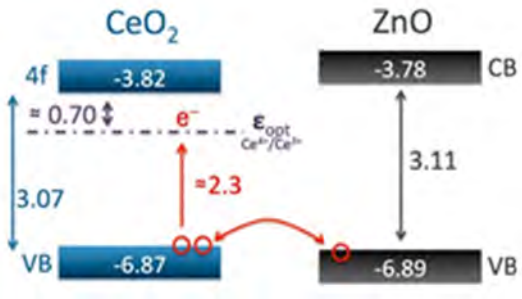

Figure 5. Schematic diagram of the final ZnO/CeO_2 band alignment and possible photoexcitation of the composite system as obtained by DFT calculations. Values are reported in eV. Reprinted with permission from [101] Copyright ACS (2018).

Concerning the topic treated in this section, the nature of the incredibly high photocatalytic yield shown by the Ce-ZnO system in the mineralization of recalcitrant compounds in wastewaters, also with pure visible light, cannot be satisfyingly described yet. The main reason lies in the quality of available data, very often only focused on the photocatalytic rate rather than on the structural and electronic features of the complex modified material. In this regard, it is not completely clear if cerium could actually enter the ZnO matrix and the photocatalytic performance doesn't seem to depending on the employed synthetic route: thus, highly sensitive structural analysis must be carried out in order to clarify this essential point and to definitely determine the working mechanism. Indeed, it seems somewhat unlikely that cerium, stabilized on ZnO surface or in crystal grain boundaries or dislocations, could just act as an electronic mediator for the photoexcited electrons from the conduction band of ZnO since that would not justify the visible light absorption. However, considering the structural and size features of Zn and Ce, the CeO_2-ZnO biphasic solid is highly likely to occur respect to a pure doped system; still, the mutual interaction of the two oxide phases at the interface appears to explain the visible light absorption, the charge carrier separation at the material interfaces and their migration at the surface to efficiently drive AOPs.

2.2. Ce-Doped ZrO_2

It is widely known that the CeO_2-ZrO_2 composite is a key component in many catalytic processes due to the excellent redox properties of the two oxides, good thermal stability and oxygen storage capability [129–131]. It has also been identified as the promoter of the so called three-way catalysts that are used to purify vehicle exhausted gases from CO, NO_x and hydrocarbons [132,133]. However, in addition to the aforementioned awareness, at the best of our knowledge, the Ce-doped ZrO_2 system arguably also represents one of the first example of the so called third-generation photoactive materials based on the double excitation through localized intraband gap states, as theorized by Serpone and Emilie [69,70]. Accordingly, this technology underpins that large band gap semiconductors or insulators, then able to absorb just UV wavelengths, such as ZrO_2, could be sensitized to visible light via introduction in the material lattice of rare earth elements. The presence of 4f orbitals would guarantee the "double photoexcitation" of electrons, namely from the valence band to *the localized f* levels, placed almost in the middle of the gap, and from these last to the conduction band. In this way, the visible light absorption would be ensured by the two-photon photoexcitation mechanism, as illustrated in Figure 6.

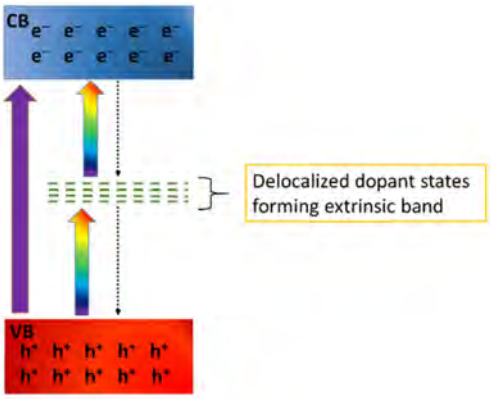

Figure 6. Mechanism of the step-by-step two-photon photoexcitation of a photoactive material through delocalized dopant states forming the extrinsic band ExB.

The great advantage that would derive from the sensitization to visible irradiation of an insulating material like ZrO_2, beyond the fact that the larger contribution in the solar spectrum is due to visible photons, is that to exploit their favourable potentials for reductive and oxidative processes; as depicted in Figure 7, the redox potentials of ZrO_2 are extremely higher in absolute value respect those of TiO_2, meaning that an electron photoexcited in the ZrO_2 CB will have a much greater potential (and then energy) to reduce a water molecule for H_2 generation. The same argument can be applied for the oxidative potentials of the photoinduced holes in the two compared oxides [134].

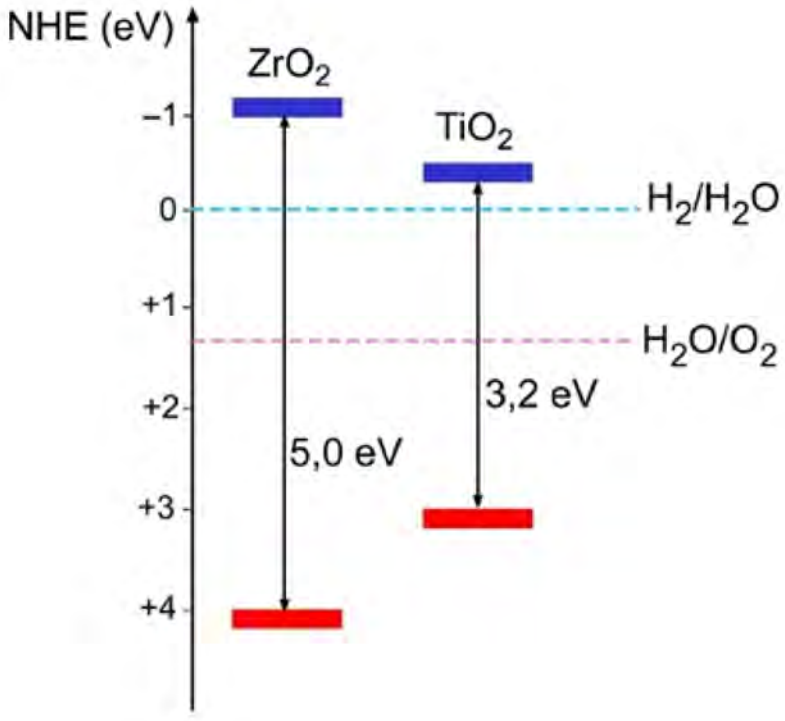

Figure 7. Relationship between the band structure of ZrO_2 and TiO_2 and the redox potential of water splitting. Reprinted with permission from [73] Copyright Elsevier (2016).

Despite the considerable benefit that such a designed material could bring in a photocatalytic process, this kind of technology still shows difficulty to be extensively applied in the photocatalytic field, probably due to the challenge in affirming with certainty the charge carrier separation and stabilization. For this reason, just a few reports have dealt with the photoactivity of Ce-doped ZrO_2 and its real-life application in the decontamination

of polluted waters upon irradiation, as reported in Table 3. It is possible to note that the in-object system has mainly exploited for the photodegradation of industrial dyes such as rhodamine-B [135–138], methylene blue [73] and Congo-red [139]; in addition, it has also tested for the abatement of humic acids [140] and phenolic compounds [138,141]. It is worth noting that all the photocatalytic measurements have been performed under visible irradiation, evidencing the highly promising photoactivity of Ce-doped ZrO_2 material.

Except in a few cases [136–138,141,142], where the amount of cerium used was extremely high (between 20% and 50%), the Ce-doped ZrO_2 substance is described as an actual doping system rather than a biphasic CeO_2-ZrO_2 heterojunction or a solid solution. As it has been asserted by many studies, the introduction of a small amount of cerium (up to 5%) in a ZrO_2 matrix stabilizes the tetragonal ZrO_2 phase at the expense of the monoclinic one, as visible in Figure 8A. Moreover, the cell parameters of the monoclinic phase are poorly influenced by the insertion of the rare earth element, while the tetragonal one has registered an increasing distortion with increasing Ce contempt [71,135]. The presence of the Ce*3d* doublets in XPS analysis attributed to the Ce^{3+} and Ce^{4+} oxidation states, once again confirmed the incorporation of cerium as an impurity in the ZrO_2 lattice [143].

The addition of the lanthanide ion also dramatically changes the optical properties of the zirconium oxide; indeed, the doped material displays a shoulder approaching the visible region that becomes progressively more intense in the UV-vis analysis with the increasing Ce percentage. In most cases, a clear red shift of the absorption edge can be observed for 5% Ce-ZrO_2, as shown in Figure 8B [72,74,140,144]. Definitely, the insertion of small percentages of cerium as an impurity within ZrO_2 causes a narrowing of the oxide band gap, converting the insulating material into a visible light-active system.

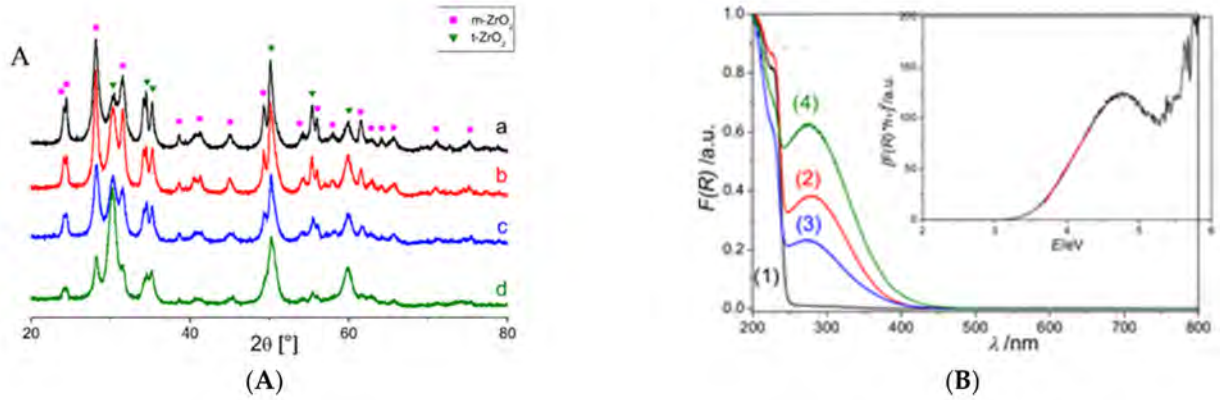

Figure 8. (**A**): XRD patterns of pure ZrO_2 (a, black) and Ce-doped ZrO_2: 0.5%mol Ce (b, red), 1%mol Ce (c, blue) and 5%mol Ce (d, green). Reprinted with permission from [135] Copyright Elsevier (2019). (**B**): Diffuse reflectance absorbance spectra of pure ZrO_2 (1, black) and Ce-doped ZrO_2: 0.5%mol Ce (2, red), 1%mol Ce (3, blue), 5%mol (4, green). Inset of panel (B): Tauc plot of 0.5%mol Ce-doped ZrO_2. Reprinted with permission from Ref. [73] Copyright Elsevier (2016).

The improved photocatalytic ability of the Ce-doped ZrO_2 system respect to that of the bare ZrO_2 results deeply connected with the increased optical response when exposed to visible wavelength irradiation, as appears from the UV-vis analysis reported above. In this regard, the experimental evidence of the pivotal role of cerium concerning the working mechanism governing the photocatalytic behaviour upon visible light of the doped system was presented by Gionco et al. These authors were able to identify a charge carrier separation under irradiation with $\lambda \geq 420$ nm by means EPR measurements at 77 K; moreover, the experimental outcomes were confirmed by DFT calculations [71–73]. Essentially, they stated that visible light photoactivity of the Ce-doped ZrO_2 can be understood thinking that the replacement of a Zr ion with a Ce ion in the same formal +4 oxidation state does not alter the charge neutrality of the system and does not result in extra electrons in the electronic structure. This occurrence causes a series of unoccupied defect states in the band gap of the oxide, at about 3–3.2 eV above the valence band edge. The unoccupied intraband

gap states were identified as the highly localized Ce *4f* orbitals. Thus, as schematized in Figure 9, where the photodegradation mechanism for the humic acid is proposed, the double jump mechanism typical of the Ce-doped ZrO_2 material suggests that the first photoexcitation step regards the promotion of electrons from ZrO_2 VB to the Ce^{4+} empty 4f states, reduced to a Ce^{3+} ion; this charge transfer process is supposed to occur at 2.5 eV, then under pure visible irradiation. In such a way, the presence of cerium favours the charge carrier separation under visible light, reducing the electron-hole pairs recombination; indeed, the electrons are stabilized on the highly localized *4f* levels. The second step excitation happens from the 4f intraband gap states to the ZrO_2 CB or to the Zr^{3+} localized states, at around 0.2 eV below the CB edge. Definitely, the photodegradation mechanism points to the role of intraband gap Ce 4f empty states, which could act as a bridge between the VB and the CB of the oxide, allowing low-energy photons to excite electrons from one band to the other.

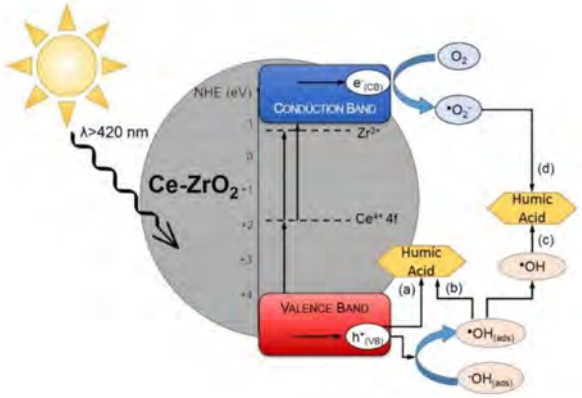

Figure 9. Proposed mechanism for the photodegradation of humic acid (HA) under visible light using Ce-ZrO_2 as photocatalyst. Reprinted from Ref. [140].

However, it is worth mentioning the disclosure presented by Zhang et al., where a $Zr_{1-x}Ce_xO_2$ (x = 0.1, 0.2, and 0.3) solid solution has been used for the decontamination from wastewater of RhB and 2,4 dichlorophenol under visible irradiation [138]. In this case, the visible light active centre was identified as being the oxo-bridged Zr^{4+}-O-$Ce^{3+/4+}$ bimetallic linkage; the co-existence of Ce^{3+} and Ce^{4+} in the solid solution was confirmed by XPS, UV–DRS, and EPR acquisitions. In details, the Ce^{3+} ions can form an Zr^{4+}–O–Ce^{3+} oxo-bridged-type complex, and this can act as a redox center via metal-to-metal electron charge transfer by irradiation of visible light, i.e., Zr^{4+}–O–Ce^{3+} ↔ Zr^{3+}–O–Ce^{4+}. At this point, the formed Zr^{3+} species can be trapped by the adsorbed oxygen molecules and retained Zr^{4+} state, which will emit the superoxide radicals. Due to high oxidation/reduction potentials, both Ce^{4+} and superoxide radicals can act as strong oxidizing agents for the degradation of organic compounds. Accordingly, in this representation scheme, the electron was accepted by the Ce^{4+} to form Ce^{3+} from the oxidized organic compound; however, a satisfying experimental evidence of the suggested mechanism still lacked.

Summarizing, the Ce-doped ZrO_2 material appears to be a real doped system with the substitution of Zr^{2+} with Ce^{4+} in the zirconia lattice positions, as variance to what is observed for Ce-ZnO. In particular, the presence of cerium stabilizes the metastable tetragonal phase at the expense of the monoclinic one, as emerged by XRD analysis and from the extrapolated lattice strain values.

Table 3. Ce concentration, structure, band gap and reaction condition used for the degradation of various pollutants for different Ce-doped ZrO_2 studies.

Synthetic Route	Ce Contempt	Structure and Morphology	E_{gap} (eV)	Irradiation Source (Power, W)	Pollutant Nature	Pollutant Concentration (mg/L)	Photocatalyst Concentration (g/L)	Best Degradation Efficiency	Ref.
Hydrothermal/Sol-gel	0.5 mol%	Mixture of Monoclinic and Tetragonal	-	Visible light (RGB-LED, 20 W)	HA	5–20	0.1–1	93% Sol-gel after 3 h	[140]
Hydrothermal	0.5–10 mol%	Mixture of Monoclinic and Tetragonal. Biphasic CeO_2-ZrO_2 for 10%	0.5%: 5.2 5%: 4 10%: 3	Visible light (SOLARBOX, 1500 W)	2-propanol	32.4	2.4	10% Ce, 100% after 2 h	[142]
Hydrothermal	0.5–5 mol%	Mixture of Monoclinic and Tetragonal	0.5%: 4.06 1%: 3.84 5%: 3.55	Visible light (RGB-LED)	RhB	10	0.7	0.5% Ce, 92% after 3 h	[135]
Hydrothermal	0.5–5 mol%	Mixture of Monoclinic and Tetragonal	0.5%: 4.06 1%: 3.84 5%: 3.55	Visible light (white-LED, 6 W)	MB	7	3	0.5% Ce, 50% after 3 h	[73]
Sol-gel	10%	Biphasic Tetragonal CeO_2-ZrO_2. Nanospheres	2.63	UV-Vis	CR	50		10% CeO_2, 70% after 2 h	[139]
Hydrothermal Microwave Mechanochemical	20%	$CeO_{0.2}ZrO_{0.8}O_2$ Solid Solution	2.8	Visible light (70 W)	RhB	4.8	1	20% CeO_2 from hydrothermal synthesis after 10 h	[136]
Hydrothermal	50%	Biphasic CeO_2-ZrO_2	-	Visible light (250 W)	RhB	4.8	0.7	40% after 150 min	[137]
Sol-gel	-	Biphasic CeO_2-ZrO_2	-	Visible light (70 W)	2-nitrophenol	50	0.8	80% after 180 min	[141]
Precipitation	1–3 mol%	$Zr_{1-x}Ce_xO2$ Solid Solution		Visible light	RhB 2,4-DCP	RhB: 4.8 2,4-DCP: 1.6	1	2% Ce, 70% after 8 h	[138]

Accordingly, the occupation of a regular crystal site by Ce^{4+} induces the formation of discrete defect levels inside the material band gap constituted by the empty localized 4f orbitals of the lanthanide ion, thus drastically improving the visible light absorption by a two-step photon absorption mechanism. Again, we highlight the importance of the sensitization of an insulating material as ZrO_2 to visible frequencies: this approach can effectively pave the way for the generation of new photocatalysts with more versatile features respect to previous ones, especially in terms of charge carrier potentials. Surely, the system needs much more investigation concerning the optimal dopant concentration, the identification of the best synthetic strategy to still improve the photodegradation yield and the exploration of different photocatalytic reactions considering also the water photo-splitting process.

3. Europium

Europium is generally used as an active red and blue emitter component in phosphorescent materials, since its reduced divalent form emits in the visible spectral range. Phosphors based on red Eu^{3+} and blue Eu^{2+} emitters, can convert UV radiation into visible light; these materials are widely employed in X-ray-intensifying screens, cathode-ray tube, or plasma-display panels, and have also been used more recently in energy-saving fluorescent lamps and light-emitting diodes [145]. On the other hand, in the last few years, these unmatched optical features have emerged as being exploitable concerning the enhancement of the visible light absorption in transition metal oxide photocatalysts.

However, being one of the least abundant rare earth elements, europium has not been extensively studied as a dopant in semiconductors for photocatalytic applications; notwithstanding, thanks to its excellent optical properties, deriving from its peculiar 4f orbitals occupation, and chemical performance, investigations of its behaviour in transition metal oxides with applications in wastewater remediation are emerging. Europium is the sixth element of the lanthanides series, with atomic number 63 and electronic configuration [Xe] $4f^7 6s^2$, showing +3 and +2 oxidation states. The unique electronic configuration, in which the 4f orbitals are occupied by one electron each, confers on Eu unparalleled luminescence properties; indeed, 4f-4f and 4f-5d transitions cause sharp radiative emissions in the UV-visible range. As presented in this section, the UV-visible light radiative emissions may be absorbed by a semiconductor in order to induced charge carrier separation and consequently to increase the photocatalytic performance of the matrix [146].

3.1. Eu-Doped ZnO

As regards Eu-doped ZnO, various synthesis routes are reported in the literature, including combustion methods, pulsed laser deposition, solid state synthesis, precipitation, hydro-solvothermal synthesis, radio frequency sputtering, sonochemical methods, microwave-assisted methods, andsol-gel methods (see Table 4) which lead to obtaining doped materials with different morphology such as thin films, spherical or desert rose-like particles, sea urchins, rods and wires, respectively [147].

A very important aspect of this novel designed system is the characterization of the synthetized material in order to understand if europium enters the crystal lattice of zinc oxide or two distinct phases are formed; this can also provide information about the parameters responsible for an enhanced sunlight-driven photocatalytic activity such as crystallite size, surface defects and band gap values. In most of the studies examined, the XRD patterns of the materials showed sharp and intense peaks of hexagonal wurtzite structure of ZnO and no europium oxide or any other impurities were observed, confirming that Eu^{3+} ions are doped into the crystal lattice of ZnO matrix. This is also corroborated by a shift to lower diffraction angles for (1 0 0), (0 0 2) and (1 0 1) planes in the Eu-doped ZnO pattern respect to the bare one, that can be explained as that the ionic radius of Eu^{3+} (0.095 nm) is much bigger than that of Zn^{2+} (0.074 nm) [144,147–155]; so the doping of Eu^{3+} ions into the ZnO matrix necessarily results in the expansion of the unit cell volume of the Eu-doped samples [151]. Peculiarly, these results seem to be frequently independent of the

type of synthesis used. However, an exception was presented by Dash et al. [156]; they prepared Eu-doped ZnO nanoparticles via soft-solution method at different concentrations of the dopant recording both a shift in XRD peak positions toward lower angle, that suggests the incorporation of Eu^{3+} ions in the lattice of ZnO, and the appearance of a small reflection traceable to a minor phase of Eu_2O_3. Babayevska et al. [157] synthetized ZnO:Eu^{3+} flower-like hierarchical structures by a template-free solvothermal method and they observed the substitution of a small number of Eu^{3+} ions in the wurtzite structure and an additional $Eu(OH)_3$ phase that increased with increasing Eu^{3+} concentration and whose presence was probably due to the incomplete reaction on addition of europium ions and to the segregation of part of the ions on the ZnO surface.

An extensive study on the nature of Eu doping in ZnO was conducted by Katea et al. [147], who through different characterization techniques (XRD, XPS, SEM, TEM) have shown how the annealing temperature used to obtain the Eu-doped sponges ZnO is decisive in determining the structure of the material. They highlighted that homogeneous, although clustered, Eu doping was achieved up to 600 °C, while phase separation into a ZnO with much lower Eu doping and Eu_2O_3 at the surface took place upon heating to higher temperatures. A similar result was obtained by Marin et al. [158], who observed the formation of Eu_2O_3 as a minor secondary phase for the sample doped with 5% of europium annealed at 800 °C. Therefore, from the analyzed references, it emerges that in the synthesis of the Eu-ZnO system the dopant Eu^{3+} partly enters in the ZnO lattice replacing Zn^{2+} and partly forms the Eu_2O_3 phase at the surface, where this occurrence is hindered by the difference in charge and size of the two ions. Thus, it can be concluded that the secondary Eu_2O_3 phase formation is observed when exceeding a critical combination of annealing temperature and doping percentage [158].

XRD data also provide valuable information on the size of the crystals formed. In general, ZnO crystals increase in size with increasing annealing temperature, but when doping with Eu, growth is inhibited.

Chandrasekhar et al. [148] observed that the crystallite size of ZnO:Eu^{3+} (9 mol%) decreased from 45 to 28 nm leading to an increase of the density of active centres on zinc oxide surface. The presence of several active centers means that the rate of interfacial charge transfer increases with a consequent enhancement of photocatalytic activity. XRD, together with Raman technique, also highlighted the expansion in the crystal lattice that creates oxygen vacancies which can also serve as electron trapping sites.

The dimensions of the crystallites and the specific surface area play an important role in determining the photocatalytic efficiency and a control over these two parameters can be exercised through the choice of the synthesis method. Franco et al. [144] compared the photocatalytic performances of Eu-doped ZnO prepared via a supercritical antisolvent process (SAS) and Eu-doped ZnO obtained by drying precipitation (DP) route monitoring the decolourization of Eriochrome Black T dye (EBT). A significant increase in UV light-driven EBT degradation was achieved using the Eu-doped ZnO sample prepared through the SAS thanks to the higher specific surface area and lower crystallite size of the material with respect to Eu-doped ZnO obtained by DP. On the other hand, the enhanced photocatalytic activity for the doped sample prepared via SAS process could also be explained considering that Eu-doped ZnO (SAS) had a wider band gap energy (E_g) than that of Eu-doped ZnO (DP) due to its smaller crystallite size, which leads to extended stability of photogenerated electron–hole pairs.

Table 4. Eu concentration, structure, morphology, band gap and reaction condition used for the degradation of various pollutants for different Eu-doped ZnO studies.

Synthetic Route	Eu Contempt	Structure and Morphology	E_{gap} (eV)	Irradiation Source (Power, W)	Pollutant Nature	Pollutant Concentration (mg/L)	Photocatalyst Concentration (g/L)	Best Degradation Efficiency	Ref.
Combustion method	3 mol %	Wurtzite Spherical, porous nanoparticles	3.15	UV (300 W)	MB	100	0.04	99.9% after 50 min	[159]
NPs by pulsed laser ablation of sintered pellets (solid-state reaction)	0.25 mol%	Wurtzite	Eu:ZnO (12 mJ, 30 min): 3.13 Eu:ZnO (68 mJ, 10 min): 3.09 Eu:ZnO (68 mJ, 15 min): 3.18	UV (240 W)	Rh6G	4.8	-	Eu:ZnO (68 mJ, 15 min): 85.4% after 45 min (42.6% for direct photolysis)	[160]
Solvothermal	1–7 at%	Wurtzite	3.28–3.17	UV (300 W)	Rh6G	50	0.4	5 at%: 50% after 110–120 min	[157]
Phyto route	1–11 mol%	Wurtzite	3.19–2.98	Natural sunlight	RhB	20	0.24	9 mol%: 94% after 60 min	[148]
Soft-solution method	0.001, 0.002 M	Wurtzite	0.001 M: 3.34 0.002 M: 3.28	UV (20 W)	MO	10	1×10^{-3}–5×10^{-3}	4 mg/L 0.002 M 90% after 180 min	[156]
Supercritical antisolvent process (1) vs. drying-precipitation method (2)	0.7 mol%	Wurtzite (1): quasi-spherical shape nanoparticles (2): desert rose-like morphology	(1): 3.22 (2): 3.21	UV (λ = 365 nm, 8 W) Vis-light (λ = 400–700 nm, 8 W)	EBT	1000	3	UV light 100% after 240 min, Vis light 22% after 240 min	[144]
Forced-hydrolysis method	0.97–3 wt.%	Wurtzite	3.30–3.34	UV-vis (20 W)	MB	8540	3	1.62% weight: 99.3% after 60 min	[149]
Sponge synthesis	0.5–10 mol%	Highly porous nanocrystalline sponges Hexagonal ZnO:Eu (or at 700–1000 °C, ZnO:Eu and cubic Eu2O3	-						[147]
Sonochemical method	1–5 mol%	Wurtzite	1%: 3.2 3%: 3.07 5%: 3.18	Vis-light (100 W)	AR17	5	1	3%Eu-ZnO: 63% after 180 min 100% adding 0.1 mM S2O82−	[150]

Table 4. *Cont.*

Synthetic Route	Eu Contempt	Structure and Morphology	E_{gap} (eV)	Irradiation Source (Power, W)	Pollutant Nature	Pollutant Concentration (mg/L)	Photocatalyst Concentration (g/L)	Best Degradation Efficiency	Ref.
Microwave assisted technique	0.1–5 mol%	Wurtzite nanorods	0.1%: 3.34 0.2%: 3.22 0.5%: 3.04	UV (λ = 365 nm)	MO	20	0.5–4	3 g/L cat, 0.2%mol Eu-ZnO: 91% after 180 min	[151]
Sponge synthesis	0.5–5%	Hexagonal zincite polymorph nanosponges	3.26	UV (λ= 350 nm, 40 W)	RhB	0.5	1	0.5%, 800 °C Annealing T: 100% after 20 min	[158]
Coprecipitation	1, 3 at%	Wurtzite	1%: 3.24 3%: 3.23	UV (λ = 254 nm, 4 W)	RhB	4	0.2	3 at% Eu^{3+}: 100% after 50 min	[152]
Sol gel	1–6 wt.%	Wurtzite thin films	1%: 3.27 4%: 3.28 6%: 3.29	UV (λ = 370 nm, 15 W)	MB	15	-	6 wt.% Eu^{3+}: 70% after 300 min	[161]
Surfactant-free chemical solution route	1–3 at%	Wurtzite Micro/nanosphere	1%: 3.21 1.5%: 3.20 2%: 3.19 3%: 3.18	Natural sunlight	Phenol	20	1	Eu (2.0 at%)/ZnO: 97.3% after 30 min	[153]
Hydrothermal synthesis	-	Wurtzite flower-like hierarchical structure	-	Natural sunlight	Phenol	-	-	92% after 60 min	[162]
Aqueous and ethanol solution synthesis	1–10%	Wurtzite Spherical nanoparticles	-	Simulated solar light (300 W)	MB, MO	10	1	ZnO:Eu(1%)-W: 90% 150 min for MB ZnO:Eu(3%)-W: 62% after 150 min for MO	[154]
Hydrothermal method	1.03–1.98%	Graphene-like nanosheets	-	UV (λ = 365 nm, 250 W)	RhB	-	-	-	[163]
Precipitation method	0.5–3%	Wurtzite nanoparticles	1 mol% Eu-ZnO: 3.31	UV (100 W)	MO	10	1	1 mol% Eu-doped ZnO:. 95.3% after 180 min	[155]

As shown in Table 4, doping with Eu usually causes a decrease in E_g with respect to pristine ZnO. As it is known, the band gap energy of the material plays a crucial role in determining the photocatalytic activity of photocatalyst since it affects the electron-hole pair recombination rate and the effectiveness under UV and visible light. The Eu-doped ZnO nanorods synthetized by Korake et al. [151] showed a remarkable absorption band edge shifted towards the longer wavelength region, which indicates a decrease of the band gap energy; they noticed that E_g gradually decreases as Eu doping increases because of the introduction of defective levels in ZnO band gap, which would act as a bridge and inducing the excitation of an electron from the valence band to the conduction band at smaller energy. This trend was confirmed by Sin et al. [153], who observed that the light absorption of Eu-doped ZnO in the visible light range was higher than that of pure ZnO and the light absorption increased with increasing the Eu content. Moreover, they evidenced a slight red shift of the optical absorption edge for all the doped products due to the narrower band gap originated from the charge transfer between the ZnO valence band and the europium ion 4f levels. Definitely, the doping of Eu can form discrete empty energy levels below the conduction band of crystalline ZnO and their presence allows a new electronic transition from the ZnO valence band to the empty energy levels of europium with less energy than ZnO valence-conduction band transition allowing Eu-doped ZnO to absorb in UV as well as in visible region of the solar light.

To highlight the advantages of doping ZnO with europium several photocatalytic experiments were performed. As in the case of materials doped with cerium, the heterogeneity of the conditions used, such as the concentration of the model pollutant, the amount of the catalyst, the reaction volumes and the type of lighting source used, make a comparison of materials in terms of performance challenging. However, a focus on the suggested degradation mechanisms and on what are the factors that influence the photocatalytic activity is proposed, since in all studies taken into account the doped systems showed higher photocatalytic activity in respect to pristine ZnO.

In general, when a semiconductor is irradiated with a photon that has energy equal or larger than its band gap, electron–hole pairs are created. The electrons are excited to conductive band (CB) and the holes are created in the valence band (VB). The recombination of the generated electron/hole pairs is one of the limiting factors as regard the efficiency of photocatalysis. However, the recombination can be reduced by metal doping, as it efficiently trap the photoinduced charge carriers and increase its mean life time [161]. In this case, europium acts as electron trap: given the standard redox potentials of $E^0(Eu^{3+}/Eu^{2+}) = -0.35$ V, $E^0(O_2/O_2^{\bullet -}) = -0.33$ V and $E_{CB}(ZnO) = -0.50$ V versus NHE, the electron is trapped to the energetically favourable Eu^{3+} ion and it is inhibited to recombine with hole. The reduced state of Eu^{2+} ions are very instable so that the electron can be easily released and transferred to ionized oxygen vacancies V_o leading to reaction with adsorbate O_2 and creation of super oxide radicals $O_2^{\bullet -}$. At the same time, the photogenerated hole can be captured on the catalyst surface undergoing interfacial charge transfer with adsorbed water molecules or with surface-bound hydroxide species to generate active $^{\bullet}$OH.

In the degradation process, pollutants are first oxidized through the successive attack of hydroxyl radical and/or through hole transfer. After oxidation, intermediates are self-degraded, or they are degraded by reactive oxidative species (ROS) to final products. Related to this aspect, one of the factors that strongly influences the photocatalytic efficiency is the percentage of europium in the catalyst.

According to most of the studies, the photodegradation efficiency first increases and then decreases with raised Eu doping. Zong et al. [155] observed the best photocatalytic activity and the largest apparent rate constant when the Eu loading was 1.0 mol%, probably because of the high efficiency for the separation of electron–hole pairs; however, above this level the photocatalytic efficiency decreased since Eu^{3+} ions may act as recombination centres for photogenerated electron–hole pairs due to their interaction.

Similar results were obtained by Sin et al. [153] who recorded the best performance with a Eu content of 2.0 at%; at low Eu content ($\leq$2.0 at%), the photocatalytic activities

increased gradually with an increase in the Eu percentage; however, increasing Eu content up to 3.0 at%, the photocatalytic activities of the products decreased. Moreover, they performed photoluminescence (PL) emission spectra with an excitation wavelength of 325 nm: it was revealed that the pure ZnO had the highest PL intensity, while the Eu (2.0 at%)-doped ZnO had the lowest one. Accordingly, a higher PL intensity indicates a higher recombination rate of the electron-hole pairs, while a lower PL intensity implies a lower recombination rate, resulting in an increase in photocatalytic performance; thus, the Eu-doped material exhibited a lower rate of the electron-hole pairs recombination and a greater photocatalytic yield. The same trend was provided by Khataee et al. [150], who sustained that, by increasing the amount of Eu into the oxide lattice, a higher surface barrier and narrower space charge layer was created with a more efficient charge carriers separation. However, if the percentage of Eu is too high, the space charge layer became very narrow and the penetration depth of light into ZnO greatly exceeded the space charge layer. This, together with an excess of the dopant covering the catalyst nanoparticles surface [149], promotes the recombination of electron–hole pairs and decreases the photocatalytic yield.

Moreover, it was rationalized that the incorporation of Eu^{3+} ions lead to an increase in the concentration of surface defects, especially O-vacancies that act as electron traps and reduce the recombination between photo-generated electron-hole pairs. If the percentage of Eu^{3+} ions and so the surface defects exceed the optimum value, also the oxygen vacancies may act as recombination centres for the photoinduced electrons and holes with a consequent reduction of the photocatalytic performance [148].

Definitely, the Eu-doped ZnO system has imposed itself as a promising catalyst for the mineralization of hazardous compounds in wastewaters driven by light absorption. Nevertheless the investigation of Eu-ZnO has received less attention than the Ce-ZnO material, the structural features and the working mechanism seem clearer. Indeed, it has emerged that the insertion of Eu ions within a ZnO matrix can be reached optimizing the dopant concentration and the annealing temperature treatment, bringing to a homogeneous system rather than a biphasic solid as for CeO_2-ZnO. In this regard, the introduction of Eu ions, with larger ionic radius, would cause a high lattice strain and large inhomogeneity in the lattice inducing smaller crystal size and higher amount of surface defects, among which oxygen vacancies represent the main ones. These lasts, coupled with the redox coupled of $Eu^{2+/3+}$ ions would guarantee a higher surface activity for the photocatalytic processes and an improved charge carrier separation, respectively, since the photoexcited electrons would be trapped in the 4f orbitals, located in the forbidden gap of ZnO. The points that still need to be clarified is the actual position of the Er ion 4f orbitals in the ZnO band gap and if their present might effectively reduce the band gap energy, allowing a two photon absorption similarly to the Ce-ZrO_2 material. Even, the luminescence properties of this lanthanide element don't seem to emerge in the considered literature, especially concerning the predicted up-conversion mechanism typical of Eu and the possibility to couple any Eu oxide phase interfaced to ZnO generating a heterojunction system as for CeO_2-ZnO.

3.2. Eu-Doped ZrO_2

The number of publications devoted to Eu-doped ZrO_2 for photodegradation applications is really limited, although considering that the unusual luminescence features of europium can in principle improve the light absorption of the large band gap of zirconia by up-converting visible light into UV frequencies.

Considering the three crystallographic phases (tetragonal, monoclinic and cubic) of ZrO_2 coupled with the large bandgap (5.0–5.85 eV) and directly linked to a high recombination rate of photogenerated electron-hole pairs, the doping with Eu have resulted in a drastic upgrading of its optical and dielectric properties [164]. In this regard, it is clear from literature data that the predominance of one crystallographic phase over the other depends on the annealing temperature and the Eu content: features of considerably importance for the evaluation of the final photocatalytic rate. Fundamentally, increasing the temperature favors the transition from the tetragonal to the thermodynamically stable monoclinic phase;

however, inserting dopants such as Eu^{3+} (similarly to the Ce-doped ZrO_2 case) lead to the metastable tetragonal phase stabilization, as indicated in Table 5. Indeed, considering that the monoclinic phase is stable when the composition is close to the stoichiometric value, the insertion of Eu^{3+} in the oxide matrix would increase the amount of oxygen vacancies bringing to the formation of the tetragonal phase [165,166]. If we consider higher temperatures, as in the case of the study conducted by Li et al. [167], the formation of the cubic phase is observed for a concentration of Eu equal to or greater than 8 mol% at 1200 °C and for a lower content of Eu (2 mol%) at 1300 °C, with a major component ratio of cubic to monoclinic with the increasing of Eu^{3+} ions content, as shown in Figure 10.

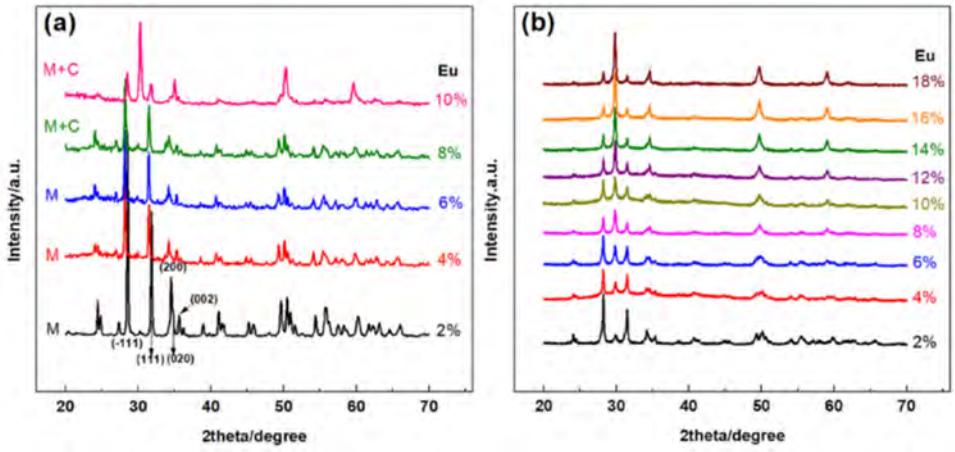

Figure 10. (**a**) The X-ray diffractions (XRD) of Eu-doped (2–10%) catalyst samples synthesized at 1200 °C, (**b**) X-ray diffractions (XRD) of Eu-doped (2–18%) catalyst samples synthesized at 1300 °C. Reprinted with permission of Ref. [167]. Copyright Elsevier 2021.

XRD analysis also shows the shift of diffraction peaks to lower angles, that becomes more evident at higher percentage of Eu because of the larger radius of Eu^{3+} (94.7 pm) than Zr^{4+} (72.8 pm), demonstrating the hosting of doping Eu ions into the crystal lattice of ZrO_2 that results in increased crystal plane spacing and unit cell volume. Moreover, the lowering of relative intensity of diffraction, together with a some degrees broadening indicates the decrease of particle size [168].

If on the one hand, the products obtained corresponding to pure cubic phase Eu-doped zirconia are not particularly efficient in photocatalytic degradation, as shown in the study by Du et al. [168], which recorded a decrease of only 28.8% of MB dye after one hour and a half of irradiation with simulated sunlight, on the other hand it is interesting to observe what happens when a monoclinic/cubic heterojunction is present.

In this regard, Li et al. [167] identified for the first time the monoclinic (M)/cubic (C) heterojunction for a 10% Eu ion contents (with an annealing temperature equal to 1200 °C). The M/C heterojunction plays a key role in the enhancement of photocatalytic degradation performance. According to the photocatalytic mechanism proposed by the authors, the existence of the monoclinic/cubic mixed phases reduces photogenerated charge carrier recombination rate since monoclinic and cubic phases show different energy band gaps including different flat band potentials. The CB and VB of cubic phase are higher than corresponding levels of monoclinic one, as shown in Figure 11. Therefore, during the photocatalytic degradation process, the photogenerated electrons in the CB of cubic phase can transfer to the CB of monoclinic one, while, oppositely, the holes in the VB of monoclinic phase can move to the VB of cubic one. Thus, the redox ability of the photocatalyst is reduced and the photogenerated electron-holes separation is promoted with consequent improving of the catalytic performance.

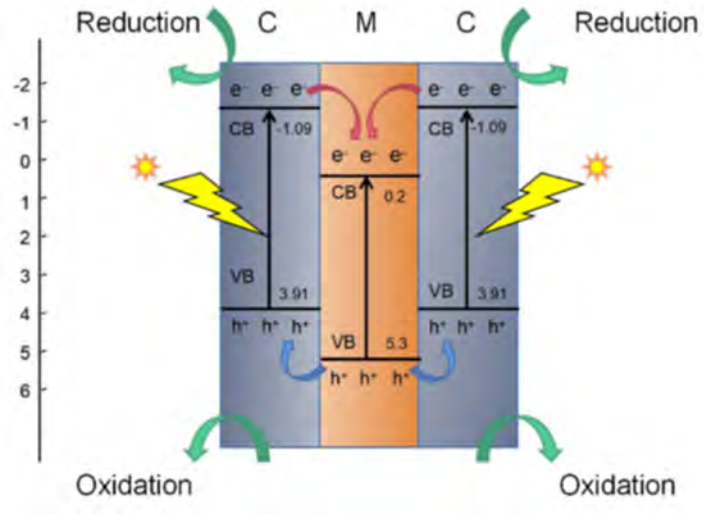

Figure 11. Schematic illustration of M/C heterophase junction charge transfer pathway. Reprinted with permission from [167]. Copyright Elsevier (2021).

In this case, the doping with Eu ions indirectly influences the photocatalytic activity, allowing to modulate the content of monoclinic and cubic phases in the catalyst.

Conversely, in the study conducted by Agorku et al. [169] the synergistic effect of Eu- and C,N,S- doping was exploited. Although C, N and S have been reported to enhance the UV-visible absorption properties of metal oxide photocatalysts, Eu^{3+} doping lead to a further increase in absorbance in the visible region and strongly contributing to the bandgap narrowing.

Finally, considering that the first paper focused on the photodegradation application of the Eu-doped ZrO_2 material just appeared in 2013, several more efforts will be needed for the evaluation of the real photocatalytic properties of this system and if it can be effectively a promising photocatalyst to be taken into account for wastewaters remediation. For instance, there is still no experimental evidence for the eventual substitution of Eu ions at the expense of a Zr^{4+} in the lattice and how the unavoidable charge compensation could affect the material properties. Still, no information is available regarding the light absorption mechanism: it might act in a similar way as the Ce-ZrO_2 material, with the 4f orbitals of Eu acting as a bridge between the ZrO_2 VB and CB for the visible light harvesting by the two-step photon absorption or if the presence of Eu can favour the pyrochlore structure, in like manner as Er-ZrO_2 (see below), thus providing a different band structure as well as photon absorption process.

Table 5. Eu concentration, structure, morphology, band gap and reaction condition used for the degradation of various pollutants for different Eu-doped ZrO_2 studies.

Synthetic Route	Eu contempt	Structure and Morphology	E_{gap} (eV)	Irradiation Source (Power, W)	Pollutant Nature	Pollutant Concentration (mg/L)	Photocatalyst Concentration (g/L)	Best Degradation Efficiency	Ref.
Coprecipitation method	0.3–1	Monoclinic (major phase) and tetragonal phases Slightly spherical shapes with distinct grain boundaries	0.3%: 2.94 0.6%: 2.99 1%: 2.91	Simulated solar light (150 W) UV filter (λ > 420 nm)	IC	20	1	0.6% Eu: 100% after 150 min	[169]
Sol-gel method	0.1–0.8 molar fraction	x(Sm/Eu)= 0.1–0.5: cubic phase, x(Sm/Eu)= 0.8, cubic phase of $RE_2Zr_2O_7$ (RE = Sm, Eu) and monoclinic structure of RE_2O_3	-	Simulated solar light (350 W)	MB, RhB	MB: 3.2 RhB: 4.8	0.4	0.2 Eu molar fraction: 28.8% after 90 min for MB	[168]
Solid state reaction method	2–10 mol% (sintered at 1200 °C) 2–18 mol% (sintered at 1300 °C)	Monoclinic and cubic phases	-	UV–vis	RhB	-	0.8	10 mol% sintered at 1200 °C: 90% after 120 min	[167]

4. Erbium

Generally, erbium has been less explored than cerium as a dopant for the enhanced heterogeneous photocatalyses exhibited by ZnO and ZrO_2. However, in our opinion, it is worth exploring and broadcasting the scientific production concerning this topic, since the peculiar optical and luminescence features characterizing this rare earth atom. Er has atomic number 68 with a [Xe] $4f^{12}6s^2$ electronic configuration; it shows almost a complete filling of the 4f orbitals, being at the end of the lanthanide series, only preceding thulium and ytterbium. The electronic configuration and the partial complete filling of the 4f orbitals bestows unique luminescence properties to the Er^{3+} ion, which similarly to the case of Eu^{3+}, don't depend on the matrix in which they are embedded, since the shielding performed by the $5s^2$ and $5p^6$ orbitals.

It has been illustrated as the absorption of 532 nm photonic radiation (then in green part of the visible region of the electromagnetic spectrum) promotes Er^{3+} ion from the ground state to the $^4S_{3/2}$ excited state, with an expected lifetime of the excited state of almost 1µs. This slightly "long" lifetime allows the population of upper state $^4D_{7/2}$ by the excited state absorption (ESA in Figure 12) process from the excited state $^4S_{3/2}$. Moreover, a no-radiative decay from the $^4D_{7/2}$ to the $^2P_{3/2}$ next lower state is also feasible. Finally, radiative transitions from the $^2P_{3/2}$ to the lower $^4D_{15/2}$ electronic state generate UV photons, as schematized in Figure 12. This kind of discrete and very selective absorptions and emissions distinctive for erbium have been already employed in high levels technology such as fiber amplifier [170] and optical atomic clocks [171]. The up-conversion of visible photons into photons of higher frequency, in the range of UV irradiation, might pay the way to a new perception of a "doped material", in which the doping agent doesn't red-shift the material band gap, but rather, it would provide the right wavelength for a higher photon absorption by the matrix.

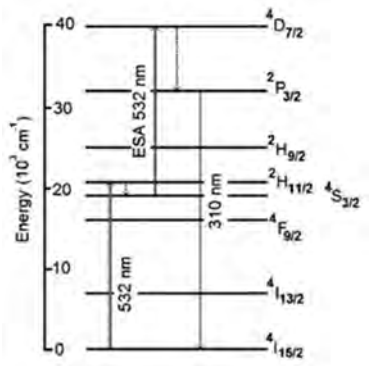

Figure 12. Simplified energy-levels diagram of Er^{3+} and excitation path for the up-conversion emission at 310 nm. Reprinted with permission of Ref. [172] Copyright Elsevier 2012.

4.1. Er-Doped ZnO

Differently from the Ce-doped ZnO system before mentioned, the Er-doped ZnO material has been less explored for the elimination of recalcitrant compounds via photocatalytic processes in polluted water. Unavoidably, this has brought to a more uncertainty about the actual action of erbium for the improvement of the photodegradation ability respect the pristine oxide. However, what emerges from the analysed literature is an enhanced photocatalytic behaviour when erbium was added in the synthesis of zinc oxide, also if, very frequently, the band gap of the final material doesn't exhibit a noticeable red-shift, as appreciable in Table 6. For this reason, the Er-modified ZnO engineered material has been mainly tested upon UV light rather than under visible photon irradiation for the mineralization of commercial dyes [173–181] and phenolic compounds [121,182,183].

From a structural point of view, most manuscripts sustain the notion of replacement of a reticular Zn^{2+} cation with a Er^{3+} cation at a regular atomic site in the lattice. This description aroused from the fact that, except in few cases [173–175], the Er_2O_3 crystal phase was

not detected via XRD or TEM analysis, also for concentration up to 5% molar [104,176,179]. Rather, it was clearly highlighted a progressive shift at lower 2θ angles of the ZnO reflection corresponding to the (111) crystallographic plane, visible in Figure 13 [175,177,178,180,182]. The systematic movement at lower 2θ with the increase of Er contempt was associated with an increasing of the lattice parameters evidenced by the analysis of the diffraction patterns. Indeed, the larger ionic radius of Er^{3+} (0.89 Å) respect to that of Zn^{2+} (0.74 Å) causes a growth of the *a* an *c* lattice parameters of the ZnO hexagonal phase and an increase of the unit cell volume; in addition, also the rise of the microstrain of the crystals would confirm the hosting of greater Er^{3+} ions in the ZnO matrix [174,178,182]. This should be also linked to the observed decreasing in the crystal size with higher Er amount: the distortion of the ZnO lattice generated by larger Er^{3+} ions would cause an inhomogeneity in the crystal habit of the matrix, thus reducing the nucleation and subsequent the growth rate of ZnO crystals. Divya and co-workers discerned between Er^{3+} in substitutional position (instead of Zn^{2+}) respect interstitial one: they declared that the increase of the lattice parameters would be generated by substitutional Er (observed at lower concentration), while the increase in the unit cell volume would occur when erbium ions occupy interstitial positions [175].

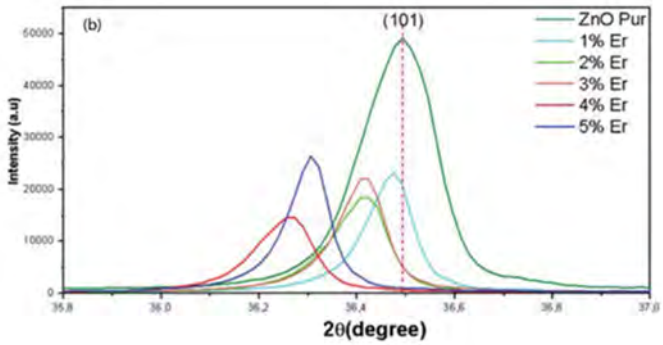

Figure 13. Evolution of the deviation of the (1 0 1) reflection for different Er-doped ZnO respect bare ZnO. Reprinted with the permission from [174]. Copyright Elsevier (2021).

As previously mentioned, the incorporation of erbium in ZnO doesn't markedly deviate the absorption edge of the prepared material respect that of ZnO; nevertheless, the optical properties of the Er-ZnO system greatly differs from that of the bare zinc oxide. Very often, the Uv-vis and photoluminescence spectroscopies highlighted the presence of erbium by means its peculiar absorptions assigned to the discrete *f-f* transitions occurring in the visible–NIR regions of the electromagnetic spectrum [104,176,182]. However, in the investigations in which a moderate red shift was detected for Er-doped ZnO it has mainly explained with an electronic transition from the valence bands to impurity levels generated by Er in substitutional position, placed just below the CB minimum. The presence of the discrete defective levels in the forbidden gap would allow the absorption of less energetic photons for the excitation of the electrons from the VB; moreover, it has been also proposed a downshift of the conduction band minimum by merging with the impurity levels. This would be in accordance with other studies concerning the gain in electron density and photocurrent values for Er-ZnO, as reported by Sordello et al. and Narayanan et al. [121,177], respectively.

Almost all the authors reported photoluminescence measurements in which the emission in the visible range (pointed in the range 550–650 nm) increases with the increase in Er content: the so called deep level emission (DLE) in ZnO is attributed to the recombination of photoinduced holes with ionized intrinsic defects generating defect levels in the material band gap, such as oxygen vacancies, zinc vacancies and zinc interstitials. This would imply that the introduction of erbium leads to a larger amount of this kind of defects that might actively participate in the charge carrier separation as electron trapping centres or directly in the photocatalytic process promoting the charge transfer at the surface of the material [174–176,179,182,184].

At least two different working mechanisms have been proposed to justify the improved photodegradation observed for Er-doped ZnO upon irradiation respect that of the pristine semiconductor, to witness the still deeply investigations required for the designed material in this research field. The first deals with the optical and luminescence properties of the Er^{3+} ion: as other lanthanide elements, erbium show unique up-conversion features, including large anti-Stokes shift, sharp emission lines and long up-conversion luminescence lifetimes (almost in the ms regime) [185]. In this way, trivalent erbium ions have the capability of efficiently converting IR radiation to UV and visible light because of favourable electronic energy levels ($^4I_{9/2}$ and $^4I_{11/2}$) [186]. Thus, Er^{3+} can absorb NIR light and simultaneously emit UV frequencies that can effectively excite the ZnO semiconductor to generate more electron-hole pairs bringing to a higher photocatalytic yeld [176]. The other provided mechanism concerns the defect levels introduce by the substitutional Er ions inside the ZnO band gap: in this case, the supplied explanation hypothesizes both a slightly reduced band gap due to the introduction of 4f defect levels at the bottom of the CB edge and the negative charge trapping by erbium ions that would act as electron scavenger, reduced to Er^{2+}. The latter is a very unstable species that immediately donates the acquired electron to an oxygen molecule, then generating superoxide radical species that could contribute to the entire photocatalytic process generating peroxide species. In such a way, the photoinduced holes in the valence band are free to oxidize an oxygen molecule or the surface OH to •OH radical, that would greatly enhance the photodegradation ability [175,177,178,180,182]. This proposed mechanism is reported in Figure 14, where the photocatalytic degradation of phenol under UV-vis irradiation by Er-ZnO quantum dots (QDs) was investigated [183].

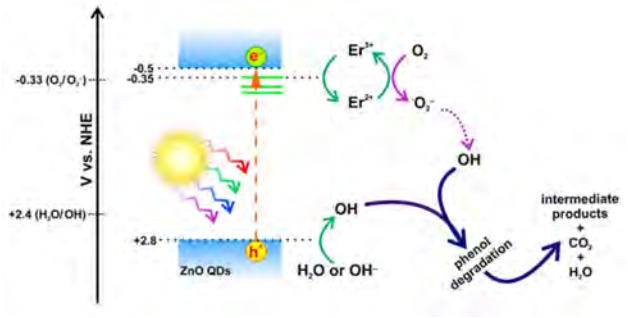

Figure 14. Proposed mechanism of phenol photocatalytic degradation in the presence of Er-doped ZnO QDs under UV–Vis irradiation. Reprinted with permission from [183]. Copyright Elsevier (2019).

Concluding, the Er-doped ZnO must be improved in order to be considered as a powerful photocatalytic material upon sunlight irradiation: in particular, light should be shed on the actual phase in which it appears in the oxide matrix, namely if in substitution of a Zn^{2+} in the lattice or in some oxidized form. Moreover, correspondingly to the Eu-ZnO compound, the up-conversion process doesn't seem efficiently improve the visible light working mechanism of the final material, even if the erbium photoluminescence fingerprints have been extensively reported: in this regard, much more synthetic routes should be explored in order to try to bring out the beneficial up-conversion mechanism operated by erbium ions. Still a systematic study of the crystal field splitting effect on the erbium ions must be performed, in order to forecast the wavelengths that can be absorbed und subsequently to rationalize if they can effectively be converted in more energetic ones.

Table 6. Er concentration, structure, morphology, band gap and reaction condition used for the degradation of various pollutants for different Er-doped ZnO studies.

Synthetic Route	Er Contempt	Structure and Morphology	E_{gap} (eV)	Irradiation Source (Power, W)	Pollutant Nature	Pollutant Concentration (mg/L)	Photocatalyst Concentration (g/L)	Best Degradation Efficiency	Ref.
Sol-gel and Spin coating	2–3.5 wt.%	Biphasic Er_2O_3-ZnO Film	-	UV-light (λ_{max} = 254 nm, 120 W)	DR-31	35	-	3% Er, 100% after 50 min	[173]
Precipitation	1–5 wt.%	Biphasic Er_2O_3-ZnO	1%: 3.29 2%: 3.27 3%: 3.29 4%: 3.28 5%: 3.23	UV-light (30 W)	RR-180	50	0.5	3% Er, 100% after 1 h	[174]
Ball Milling	0.3–1.2 wt.%	Wurtzite Biphasic Er_2O_3-ZnO for 1.2% Er	-	UV-light (λ_{max} = 380 nm, 90 W)	MB	3.2	2	0.6% Er, 100% after 25 min	[175]
Hydrothermal	1–4 mol%	Wurtzite Dumbbell		Vis-light ($\lambda \geq$ 400 nm, 350 W)	Tartaric Acid	20	0.5	4% Er, 50% after 400 min	[176]
Spray Pyrolysis	0.5–1.5 at%	Wurtzite Film	0.5%: 3.288 1%: 3.256 1.5%: 3.282	UV-light (λ_{max} = 365 nm, 15 W)	RhB	0.1	-	1% Er, 100% after 2 h	[177]
Electrospinning	1 mol%	Wurtzite Ultrathin-Fibers	2.82 eV	UV-light (150 W)	CR	30	0.33	80% after 250 min	[178]
Sol-gel	5 mol%	Wurtzite	2.74	Vis-light ($\lambda \geq$ 400 nm, 500 W)	MB	10	1	80% after 10 min	[179]
Precipitation	3.5 at%	Wurtzite Spherical	-	Vis-light	Ph	-	-	95% after 300 min	[182]
Hydrothermal	1 mol%	Wurtzite		UV-light (λ_{max} = 365 nm, 40 W)	Ph	20	1	98% after 1 h	[121]
Sol-gel	0.09–0.45 mol%	Wurtzite Quantum Dots	-	UV-Vis (1000 W)	Ph	20	0.5	0.18% Er, 90% after 1 h	[183]
Precipitation	2.1–6.3 wt.%	Wurtzite	-	UV-light (32 W)	MB	10	0.5	4.8% Er, 97.7% after 1 h	[180]
Chemical Solution Deposition	0.5–2 wt.%	Wurtzite Nanoflakes	-	UV-light (λ_{max} = 365 nm, 250 W)	RhB	5	-	1% Er, 90% after 1 h	[181]

4.2. Er-Doped ZrO_2

Just a couple of reports have been published dealing with the application of the Er-doped ZrO_2 system for the abatement of harmful substances via photocatalytic processes. However, in our opinion, this technology should receive much more attention due to the possibility of providing an alternative third-generation photocatalysts, as tentatively outlined for the Ce-doped ZrO_2 material. One of the possible reasons why the Er-doped ZrO_2 system didn't enjoy the same fortune of the relative Ce-doped ZrO_2 material is probably that in some cases the introduction of also small amounts of erbium in ZrO_2 brought to a lower photocatalytic activity both under UV and visible irradiation. As we will try to describe, the presence of 4f levels in ZrO_2 arising from the presence of Er^{3+} could actually behave as recombination centres, thus inhibiting a proficient charge carriers separation process, essential for a promising photocatalytic applications.

The major part of the synthetic methods proposed are hydrothermal ones. This might be explained considering that the hydrothermal synthesis route leads to a high crystallinity of the prepared nanoparticles. A higher crystallinity is very often associated with a higher photocatalytic activity since the photoinduced electron-hole pairs can no longer migrate in the solid reducing the recombination rate. In this regard, the hydrothermally prepared Er-doped ZrO_2 nanostructure have been employed for the photo-oxidation of 2-propanol and the photodegradation of MB and RhD under both LED and UV-vis light irradiation [74,140,147], as reported in Table 7. Despite the discrete degradation ability upon light irradiation, they represent promising leads for the investigation of visible light photoactive materials for photocatalytic applications based on wide band gap semiconducting/insulating materials.

XRD analysis have revealed that the insertion of Er^{3+} ions within ZrO_2 matrix stabilizes the tetragonal phase at the expense of the monoclinic one, as evidenced in Figure 15A [73,142], Moreover, Rietveld analysis showed that the monoclinic crystal structure is poorly influenced by the erbium incorporation while it registered a distortion of the tetragonal lattice parameters [135].

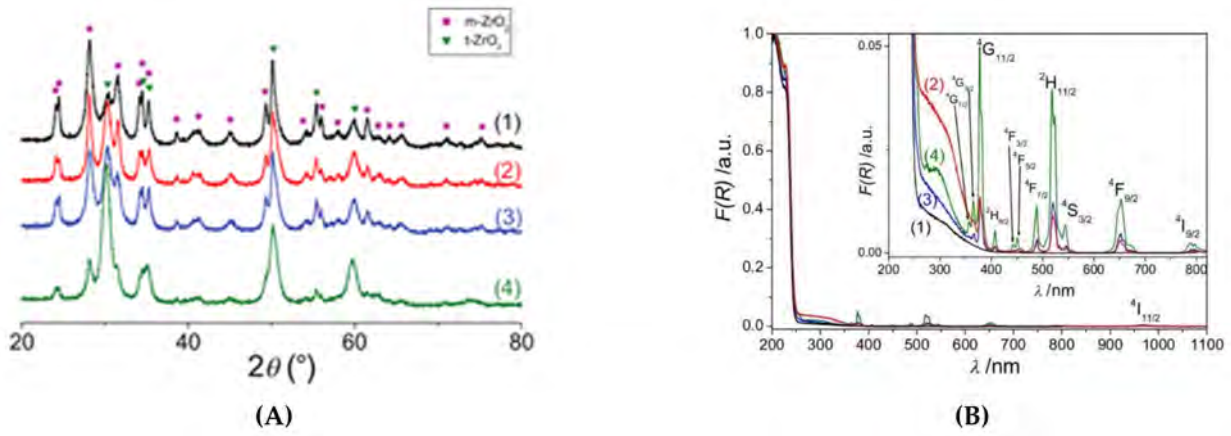

Figure 15. (**A**): XRD patterns of (1) pure ZrO_2 (black) and Er-doped ZrO_2 with increasing concentration of Er contempt: (2) 0.5 mol% (red), (3) 1 mol% (blue) and (4) 5 mol% (green). (**B**): Diffuse reflectance absorbance spectra of (1) pure ZrO_2 (black) and Er-doped ZrO_2 with increasing concentration of Er contempt: (2) 0.5 mol% (red), (3) 1 mol% (blue) and (4) 5 mol% (green). Reprinted with permission from [73] Copyright Elsevier (2016).

Only Tong et al. have synthesized via a precipitation method an Er-ZrO_2 system containing the Er:Zr ratio 1:1; In this case, XRD analysis evidenced the presence of the fluorite-type pyrochloric structure typical of the $Er_2Zr_2O_7$ solid solution. They performed the photocatalytic abatement in aqueous media of the methyl orange dye under purely visible light irradiation evidencing how the solid solution was more active than bare ZrO_2 in the degradation process. They connected the enhanced photocatalytic ability to the

magnetic moment characterizing the lanthanide element that would improve the charge carrier separation.

The absorption edge of the Er-modified zirconium dioxide evidenced any change respect that of the bare oxide, exhibiting an absorption centred at 290 nm; thus, a red-shift due to the introduction of erbium species in the matrix was not recorded. However, the optical features of ZrO_2 are dramatically affected by the presence of erbium, as shown in Figure 15B: indeed, a multitude of selective absorption bands appeared, with higher intensity increasing with the rise up of the Er amount [74,140,148]. The preservation of the optical properties of Er^{3+} indicates a good dilution of the element in the oxide matrix. In addition, a weaker absorption is also present around 350 nm, attributed to oxygen vacancies in ZrO_2 caused by the presence of Er; PL analysis confirmed this hypothesis [142].

XPS spectroscopy helped in the understanding the electronic character of the material: it was highlighted that the engineered material behaves as *a p-type* semiconductor with the presence of acceptor impurities induced by the insertion of erbium in the matrix. One possibility is the presence of interstitial oxygen in the monoclinic ZrO_2, which creates shallow traps near the valence band maximum [135].

The unique working mechanism appearing for this system is the one provided by Hernández et al., where they modelled a heterojunction between the monoclinic and tetragonal ZrO_2 phases, represented in Figure 16. The presence of the 4f orbitals in both the tetragonal and monoclinic crystal phases of ZrO_2 due to the Er cations would favour the charge carriers\ separation and the improvement of light harvesting. Moreover, the charge transfer at the interface would also delay and limit the electron-hole pairs recombination [143].

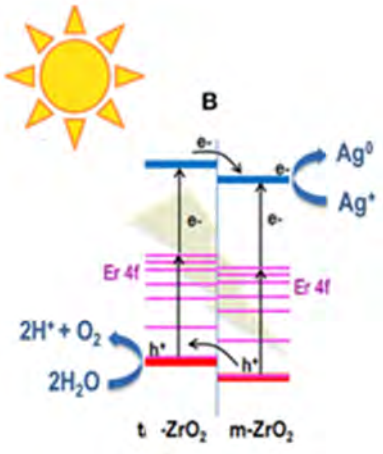

Figure 16. Scheme of solar-driven photocatalytic water oxidation in the presence of Ag^+ as electron scavenger under sunlight illumination over the Er-doped ZrO_2 sample, where it is evident the enhanced charges separation due to the presence of two ZrO_2 polymorphs. Reprinted with permission from [143] Copyright Frontiers (2018).

The limited literature available for the Er-doped ZrO_2 system should encourage further in-depth investigations and characterization of the promising material for photodegradation processes. For instance, the role of the dopant in the ZrO_2 phases (substitutional or interstitial) remains an open question. Still, the precipitation of the pyrochloric $Er_2Zr_2O_7$ solid solution might bring to a further enhance of the photocatalytic ability upon visible irradiation. Again, the peculiar Er^{3+} electronic configuration should be evaluated in light of the crystal field splitting in order to both better understand the possible shallow acceptor trap levels suggested by some authors and the opportunity to exploit the up-conversion process, typical of this element.

Table 7. Er concentration, structure, morphology, band gap and reaction condition used for the degradation of various pollutants for different Er-doped ZrO_2 studies.

Synthetic Route	Er Contempt	Structure and Morphology	E_{gap} (eV)	Irradiation Source (Power, W)	Pollutant Nature	Pollutant Concentration (mg/L)	Photocatalyst Concentration (g/L)	Best Degradation Efficiency	Ref.
Hydrothermal	0.5–10 mol%	Tetragonal and Monoclinic	0.5%: 5.2 5%: 5.1	UV-vis (λ_{max} = 365 nm, 1500 W)	2-propanol	32	2.4	0.5% Er, 30% after 250 min	[142]
Hydrothermal	0.5–5 mol%	Tetragonal and Monoclinic	0.5%: 5.13 1%: 5.13 5%: 5.12	LED (λ_{max} = 475 nm, 200 W)	MB	7	3	0.5% Er, 30% after 3 h	[73]
Hydrothermal	0.5–5 mol%	Tetragonal and Monoclinic	0.5%: 5.13 1%: 5.13 5%: 5.12	UV-vis	RhB	10	0.7	0.5% Er, 80% after 3 h	[135]
Precipitation	50 mol%	Fluorite type $Er_2Zr_2O_7$ Pyrochloric	-	UV light (λ_{max} = 365 nm, 300 W)	MO	20	1	87% after 2 h	[187]

5. Conclusions

In this review, the effect on the structural, optical and electronic features of ZnO and ZrO_2 of cerium, europium and erbium has been extensively explored and connected to the higher photocatalytic activity respect to the unmodified materials. It has been highlighted how the different nature and thus 4f orbital filling of the employed lanthanides can differently affect the transition metal oxide properties, providing a higher pollutant abatement in wastewater. Particularly, we focused attention on the alteration of both defect and electronic structure induced by cerium, europium and erbium introduction in the oxide matrixes and how their presence, in the lattice or on the material surface, impacts the photon absorption and the surface-bulk charge carrier dynamics. Specifically, we highlighted how for the nature of the various lanthanides, deriving from the 4f orbital filling, different phenomena are expected: accordingly, for Eu and Er, differently from Ce, already show occupation of the 4f levels, the up-conversion process is expected to improve the visible light absorption, at least in theory. On the other hand, it emerges that it is difficult to definitely exploit this kind of fine procedure, at least at the best of the technology reached until now concerning the synthetic routes coupled with the lack of a complete understanding of the overall phenomena. Probably some other occurrences should be taken into account such as the crystal field splitting effect related to a specific point symmetry in a given crystal structure in determining the energy distance between the excited states and the ground state; this would also affect the lifetime of the photoinduced electrons in the 4f excited states thus completely changing the up-conversion process expected for the isolated ion. Thus, up to now, there is no clear and satisfying experimental evidence of the actual occurrence of the up-conversion process for the proposed materials: however, as emphasized, more careful analysis of the electronic properties of the overall final material can definitely shed the light on this technology that can effectively greatly improve the photocatalytic yield of this material, with particular reference on the visible photon absorption.

We systematically present, by means of tables, the synthesis procedures with which the presented novel materials were synthetized, evidencing the dopant percentage, the resulted crystal structure and band gap value as well as the best photodegradation ability for each study. Deep considerations have been done for the doping amount, dwelling on its structural and electronic role. In some cases, the lanthanide is believed to be hosted in the oxide lattice, while in others it clearly forms a segregated phase at the oxide surface; this clearly greatly affects the material working mechanism upon irradiation, the generation of the hydroxyl species and the final contaminant annihilation.

The analysed literature works, although characterized by different explanations, often in contradiction with each other, revealed a surprising enhanced of the photoacatlytic ability of the engineered oxides, recording for the last a higher amount of hydroxyl, superoxide and peroxo species produced. Among all the considered materials, Ce-ZnO and Ce-ZrO_2 provide the best photocatalysts, also considering pure visible light illumination, for the mineralization of hazardous compounds in wastewaters. They also are a clear and fascinating example of the different role of the same lanthanides in the two oxide matrices: while Ce forms a segregated phase in ZnO, constituting the CeO_2-ZnO heterojunction, able to drastically reduce the charge carriers recombination, it substitutes a Zr^{4+} in ZrO_2 in a regular lattice site, introducing discrete defect levels in the material band gap, allowing the absorption of visible light via the two step photon absorption mechanism and accounting as one of the first example of third-generation photocatalysts.

Along all the manuscripts, our work has aimed to homogenise the recorded outcomes trying to provide the most satisfying models able to describe the light absorption processes and oxidative active species formation for each lanthanides-modified ZnO and ZrO_2, with the aim to induce future researches of relevance in the field. Indeed, the data presented in the literature doesn't often deal with the real role of the lanthanides and how they actually act in the improvement of the photodegradation yield: these information are of paramount importance for the development of even more efficient semiconductors. In

the next future, the synergic employment of different high-resolution techniques coupled with the nowadays highly-performance computational calculations must be considered for a more realistic interpretation of the lanthanides-engineered materials, for the urgent production of a reliable technology for the wastewater treatment. In particular, as widely commented, a systematic investigation of the crystal field splitting depending on the site occupied by the lanthanide ions would greatly help in understanding and expecting the behaviour of the lanthanide inside the oxide matrix.

Author Contributions: Conceptualization, P.C., M.C.P. and E.C.; methodology, E.G. and E.C., investigation, E.G. and E.C.; writing—original draft preparation E.G. and E.C., writing—review and editing E.C.; supervision, P.C., M.C.P. and E.C.; project administration P.C. and M.C.P. All authors have read and agreed to the published version of the manuscript.

Funding: Financial support from the European Union's Horizon 2020 research and innovation programme under the Marie Skłodowska-Curie grant agreement no. 765860 (AQUAlity), from the European Union's Horizon 2020 research and innovation programme under the Marie Skłodowska-Curie grant agreement No 101007578" (SusWater) and from the Italian MIUR through the PRIN Project 20179337R7, MULTI-e "Multielectron transfer for the conversion of small molecules: an enabling technology for the chemical use of renewable energy.

Institutional Review Board Statement: Not applicable.

Informed Consent Statement: Not applicable.

Data Availability Statement: Not applicable.

Acknowledgments: This paper is part of a project that has received funding from the European Union's Horizon 2020 research and innovation programme under the Marie Skłodowska-Curie grant agreement no. 765860 (AQUAlity), from the European Union's Horizon 2020 research and innovation programme under the Marie Skłodowska-Curie grant agreement No 101007578" (SusWater) and from the Italian MIUR through the PRIN Project 20179337R7, MULTI-e "Multielectron transfer for the conversion of small molecules: an enabling technology for the chemical use of renewable energy".

Conflicts of Interest: The authors declare no conflict of interest.

References

1. UNICEF. *Progress on Household Drinking Water, Sanitation and Hygiene 2000–2017. Special Focus on Inequalities*; UNICEF: New York, NY, USA, 2019.
2. Alharbi, O.M.L.; Basheer, A.A.; Khattab, R.A.; Ali, I. Health and Environmental Effects of Persistent Organic Pollutants. *J. Mol. Liq.* **2018**, *263*, 442–453. [CrossRef]
3. Sauvè, S.; Desrosiers, M. A Review of What is an Emerging Contaminant. *Chem. Cent. J.* **2014**, *8*, 15. [CrossRef]
4. Rizzo, L.; Malato, S.; Antakyali, D.; Beretsou, V.G.; Dolic, M.B.; Gernjak, W.; Heath, E.; Ivancev-Tumbas, I.; Karaolia, P.; Lado Ribeiro, A.R.; et al. Consolidated vs New Advanced Treatment Methods for the Removal of Contaminants of Emerging Concern from Urban Wastewater. *Sci. Total Environ.* **2019**, *655*, 986–1008. [CrossRef] [PubMed]
5. Rivera-Utrilla, J.; Sanchez-Polo, M.; Ferro-Garcia, M.A.; Prados-Joya, G.; Ocampo-Perez, R. Pharmaceuticals as Emerging Contaminants and their Removal from Water. A Review. *Chemosphere* **2013**, *93*, 1268–1287. [CrossRef] [PubMed]
6. Konstantinou, I.K.; Albanis, T.A. TiO2-Assisted Photocatalytic Degradation of Azo Dyes in Aqueous Solution: Kinetic and Mechanistic Investigations. *Appl. Catal. B* **2004**, *49*, 1–14. [CrossRef]
7. Santiago-Morales, J.; Gomez, M.J.; Herrera-Lopez, S.; Fernandez-Alba, A.R.; García-Calvo, E.; Rosal, R. Energy Efficiency for the Removal of non-Polar Pollutants during Ultraviolet Irradiation, Visible Light Photocatalysis and Ozonation of a Wastewater Effluent. *Water Res.* **2013**, *47*, 5546–5556. [CrossRef] [PubMed]
8. Paździor, K.; Bilińska, L.; Ledakowicz, S. A Review of the Existing and Emerging Technologies in the Combination of AOPs and Biological Processes in Industrial Textile Wastewater Treatment. *Chem. Eng. J.* **2019**, *376*, 120597. [CrossRef]
9. Mo, J.; Hwang, J.-E.; Jegal, J.; Kim, J. Pretreatment of a Dyeing Wastewater using Chemical Coagulants. *Dyes Pigm.* **2007**, *72*, 240–245. [CrossRef]
10. Mo, J.H.; Lee, Y.H.; Kim, J.; Jeong, J.Y.; Jegal, J. Treatment of Dye Aqueous Solutions using Nanofiltration Polyamide Composite Membranes for the Dye Wastewater Reuse. *Dyes Pigm.* **2008**, *76*, 429–434. [CrossRef]
11. Ince, N.H.; Gönenç, D.T. Treatability of a Textile Azo Dye by UV/H_2O_2. *Environ. Technol.* **1997**, *18*, 179–185. [CrossRef]
12. Jain, S.N.; Gogate, P.R. Efficient Removal of Acid Green 25 Dye from Wastewater using Activated Prunus Dulcis as Biosorbent: Batch and Column Studies. *J. Environ. Manage.* **2018**, *210*, 226–238. [CrossRef] [PubMed]

13. Cuerda-Correa, E.M.; Alexandre-Franco, M.F.; Fernández-González, C. Advanced Oxidation Processes for the Removal of Antibiotics from Water. An Overview. *Water* **2019**, *12*, 102. [CrossRef]
14. Kang, S.; Liao, C.; Po, S. Decoloration of Texile Wastewater by Photo-fenton Oxidation Technology. *Chemosphere* **2000**, *41*, 1287–1294. [CrossRef]
15. O'Shea, K.E.; Dionysiou, D.D. Advanced Oxidation Processes for Water Treatment. *J. Phys. Chem. Lett.* **2012**, *3*, 2112–2113. [CrossRef]
16. Gorito, A.M.; Lado Ribeiro, A.R.; Pereira, M.F.R.; Almeida, C.M.R.; Silva, A.M.T. Advanced Oxidation Technologies and Constructed Wetlands in Aquaculture farms: What do we know so far about Micropollutant Removal? *Environ. Res.* **2021**, *204*, 111955. [CrossRef] [PubMed]
17. Ganiyu, S.O.; Sable, S.; Gamal El-Din, M. Advanced Oxidation Processes for the Degradation of Dissolved Organics in Produced Water: A Review of Process Performance, Degradation Kinetics and Pathway. *Chem. Eng. J.* **2022**, *429*, 132492. [CrossRef]
18. Azbar, N.; Yonar, T.; Kestioglu, K. Comparison of Various Advanced Oxidation Processes and Chemical Treatment Methods for COD and Color Removal from a Polyester and Acetate Fiber Dyeing Effluent. *Chemosphere* **2004**, *55*, 35–43. [CrossRef]
19. Oturan, M.A.; Aaron, J.J. Advanced Oxidation Processes in Water/Wastewater Treatment: Principles and Applications. A review. *Crit. Rev. Environ. Sci. Technol.* **2014**, *44*, 2577–2641. [CrossRef]
20. Chan, S.H.S.; Yeong Wu, T.; Juan, J.C.; Teh, C.Y. Recent Developments of Metal Oxide Semiconductors as Photocatalysts in Advanced Oxidation Processes (AOPs) for Treatment of Dye Waste-Water. *J. Chem. Technol. Biotechnol.* **2011**, *86*, 1130–1158. [CrossRef]
21. Anwer, H.; Mahmood, A.; Lee, J.; Kim, K.-H.; Park, J.-W.; Yip, A.C.K. Photocatalysts for Degradation of Dyes in Industrial Effluents: Opportunities and Challenges. *Nano Res.* **2019**, *12*, 955–972. [CrossRef]
22. Malato, S.; Fernández-Ibáñez, P.; Maldonado, M.I.; Blanco, J.; Gernjak, W. Decontamination and Disinfection of Water by Solar Photocatalysis: Recent Overview and Trends. *Catal. Today* **2009**, *147*, 1–59. [CrossRef]
23. Patial, S.; Kumar, R.; Raizada, P.; Singh, P.; Van Le, Q.; Lichtfouse, E.; Le Tri Nguyen, D.; Nguyen, V.H. Boosting Light-driven CO_2 Reduction into Solar Fuels: Mainstream Avenues for Engineering ZnO-based Photocatalysts. *Environ. Res.* **2021**, *197*, 111134. [CrossRef] [PubMed]
24. Hoffmann, R.M.; Martin, S.T.; Choi, W.; Bahnemann, D.W. Environmental Applications of Semiconductor Photocatalysis. *Chem. Rev.* **1995**, *95*, 69–96. [CrossRef]
25. Ollis, D.F.; Pelizzetti, E.; Serpone, N. Destruction of Water Contaminants. *Environ. Sci. Technol.* **1991**, *25*, 1522–1529. [CrossRef]
26. Mills, A.; Hunte, S.L. An Overview of Semiconductor Photocatalysis. *J. Photochem. Photobiol. A* **1997**, *108*, 1–35. [CrossRef]
27. Ahmed, S.; Rasul, M.G.; Brown, R.; Hashib, M.A. Influence of Parameters on the Heterogeneous Photocatalytic Degradation of Pesticides and Phenolic Contaminants in Wastewater: A Short Review. *J. Environ. Manage.* **2011**, *92*, 311–330. [CrossRef]
28. Valadez-Renteria, E.; Oliva, J.; Rodriguez-Gonzalez, V. Photocatalytic Materials immobilized on Recycled supports and their Role in the Degradation of Water Contaminants: A timely Review. *Sci. Total Environ.* **2021**, *807*, 150820. [CrossRef] [PubMed]
29. Hashimoto, K.; Irie, H.; Fujishima, A. TiO_2 Photocatalysis: A Historical Overview and Future Prospects. *Jpn. J. Appl. Phys.* **2005**, *44*, 8269–8285. [CrossRef]
30. Aremu, O.H.; Akintayo, C.O.; Naidoo, E.B.; Nelana, S.M.; Ayanda, O.S. Synthesis and Applications of Nano-sized Zinc Oxide in Wastewater Treatment: A Review. *Int. J. Environ. Sci. Technol.* **2021**, *18*, 3237–3256. [CrossRef]
31. Kumar, S.G.; Rao, K.S.R.K. Zinc Oxide based Photocatalysis: Tailoring Surface-bulk Structure and Related Interfacial Charge Carrier Dynamics for Better Environmental Applications. *RSC Adv.* **2015**, *5*, 3306–3351. [CrossRef]
32. Ani, I.J.; Akpan, U.G.; Olutoye, M.A.; Hameed, B.H. Photocatalytic Degradation of Pollutants in Petroleum Refinery Wastewater by TiO_2- and ZnO-based Photocatalysts: Recent Development. *J. Cleaner Prod.* **2018**, *205*, 930–954. [CrossRef]
33. Medhi, R.; Marquez, M.D.; Lee, T.R. Visible-Light-Active Doped Metal Oxide Nanoparticles: Review of their Synthesis, Properties, and Applications. *ACS Appl. Nano Mater.* **2020**, *3*, 6156–6185. [CrossRef]
34. Friedmann, D.; Mendive, C.; Bahnemann, D. TiO2 for Water Treatment: Parameters Affecting the Kinetics and Mechanisms of Photocatalysis. *Appl. Catal. B* **2010**, *99*, 398–406. [CrossRef]
35. Gaya, U.I.; Abdullah, A.H. Heterogeneous Photocatalytic Degradation of Organic Contaminants over Titanium Dioxide: A Review of Fundamentals, Progress and Problems. *J. Photochem. Photobiol. C* **2008**, *9*, 1–12. [CrossRef]
36. Ong, C.B.; Ng, L.Y.; Mohammad, A.W. A Review of ZnO Nanoparticles as Solar Photocatalysts: Synthesis, Mechanisms and Applications. *Renew. Sustain. Energy Rev.* **2018**, *81*, 536–551. [CrossRef]
37. Abdullah, F.H.; Bakar, N.; Bakar, M.A. Current Advancements on the Fabrication, Modification, and Industrial Application of Zinc Oxide as Photocatalyst in the Removal of Organic and Inorganic Contaminants in Aquatic Systems. *J. Hazard. Mater.* **2021**, *424*, 127416. [CrossRef] [PubMed]
38. Goktas, S.; Goktas, A. A Comparative Study on Recent Progress in Efficient ZnO based Nanocomposite and Heterojunction Photocatalysts: A Review. *J. Alloys Compd.* **2021**, *863*, 158734. [CrossRef]
39. Ikram, M.; Rashid, M.; Haider, A.; Naz, S.; Haider, J.; Raza, A.; Ansar, M.T.; Uddin, M.K.; Ali, N.M.; Ahmed, S.S.; et al. A Review of Photocatalytic Characterization, and Environmental Cleaning, of Metal Oxide Nanostructured Materials. *Sustain. Mater. Technol.* **2021**, *30*, e00343. [CrossRef]
40. Verma, S.; Younis, S.A.; Kim, K.H.; Dong, F. Anisotropic ZnO Nanostructures and their Nanocomposites as an Advanced Platform for Photocatalytic Remediation. *J. Hazard. Mater.* **2021**, *415*, 125651. [CrossRef] [PubMed]

41. Kumar, S.; Ojha, A.K. Oxygen Vacancy Induced Photoluminescence Properties and Enhanced Photocatalytic Activity of Ferromagnetic ZrO_2 Nanostructures on Methylene Blue Dye under Ultra-Violet Radiation. *J. Alloys Compd.* **2015**, *644*, 654–662. [CrossRef]
42. Fang, D.; Luo, Z.; Liu, S.; Zeng, T.; Liu, L.; Xu, J.; Bai, Z.; Xu, W. Photoluminescence Properties and Photocatalytic Activities of Zirconia Nanotube Arrays Fabricated by Anodization. *Opt. Mater.* **2013**, *35*, 1461–1466. [CrossRef]
43. Zheng, H.; Liu, K.; Cao, H.; Zhang, X. L-Lysine-Assisted Synthesis of ZrO_2 Nanocrystals and Their Application in Photocatalysis. *J. Phys. Chem. C* **2009**, *113*, 18259–18263. [CrossRef]
44. Hassan, N.S.; Jalil, A.A. A Review on Self-modification of Zirconium Dioxide Nanocatalysts with Enhanced Visible-Light-driven Photodegradation of Organic Pollutants. *J. Hazard. Mater.* **2021**, *423*, 126996. [CrossRef] [PubMed]
45. Folli, A.; Bloh, J.Z.; Strom, M.; Madsen, T.P.; Henriksen, T.; Macphee, D.E. Efficiency of Solar-Light-Driven TiO_2 Photocatalysis at Different Latitudes and Seasons. Where and When Does TiO_2 Really Work? *J. Phys. Chem. Lett.* **2014**, *5*, 830–832. [CrossRef]
46. Lee, K.M.; Lai, C.W.; Ngai, K.S.; Juan, J.C. Recent Developments of Zinc Oxide Based Photocatalyst in Water Treatment Technology: A Review. *Water Res.* **2016**, *88*, 428–448. [CrossRef]
47. Samadi, M.; Zirak, M.; Naseri, A.; Khorashadizade, E.; Moshfegh, A.Z. Recent Progress on Doped ZnO Nanostructures for Visible-Light Photocatalysis. *Thin Solid Film.* **2016**, *605*, 2–19. [CrossRef]
48. Khaki, M.R.D.; Shafeeyan, M.S.; Raman, A.A.A.; Daud, W. Application of Doped Photocatalysts for Organic Pollutant Degradation—A Review. *J. Environ. Manage.* **2017**, *198*, 78–94. [CrossRef]
49. Basavarajappa, P.S.; Patil, S.B.; Ganganagappa, N.; Reddy, K.R.; Raghu, A.V.; Reddy, C.V. Recent Progress in Metal-doped TiO_2, non-Metal Doped/Codoped TiO_2 and TiO_2 Nanostructured Hybrids for Enhanced Photocatalysis. *Int. J. Hydrog. Energy* **2020**, *45*, 7764–7778. [CrossRef]
50. Wang, Y.; Wang, Q.; Zhan, X.; Wang, F.; Safdar, M.; He, J. Visible light driven type II heterostructures and their enhanced photocatalysis properties: A review. *Nanoscale* **2013**, *5*, 8326–8339. [CrossRef] [PubMed]
51. Low, J.; Yu, J.; Jaroniec, M.; Wageh, S.; Al-Ghamdi, A.A. Heterojunction Photocatalysts. *Adv. Mat.* **2017**, *29*, 16011694. [CrossRef]
52. Nemiwal, M.; Zhang, T.C.; Kumar, D. Recent Progress in g-C_3N_4, TiO_2 and ZnO based Photocatalysts for Dye Degradation: Strategies to Improve Photocatalytic Activity. *Sci. Total Environ.* **2021**, *767*, 144896. [CrossRef]
53. Cerrato, E.; Paganini, M.C. Mechanism of Visible Photon Absorption: Unveiling of the C_3N_4–ZnO Photoactive Interface by means of EPR Spectroscopy. *Mater. Adv.* **2020**, *1*, 2357. [CrossRef]
54. Xu, Q.; Zhang, L.; Yu, J.; Wageh, S.; Al-Ghamdi, A.A.; Jaroniec, M. Direct Z-Scheme Photocatalysts: Principles, Synthesis, and Applications. *Mater. Today* **2018**, *21*, 1042–1063. [CrossRef]
55. Cerrato, E.; Rebolini, E.; Fabbri, D.; Calza, P.; Paganini, M.C. Ternary Systems based on ZnO/CeO_2/Cu_2O for the Degradation of Phenol and Carbamazepine. *J. Alloys Compd.* **2021**, *856*, 158167. [CrossRef]
56. Liu, X.; Iocozzia, J.; Wang, Y.; Cui, X.; Chen, Y.; Zhao, S.; Li, Z.; Lin, Z. Noble Metal–Metal Oxide Nanohybrids with Tailored Nanostructures for Efficient Solar Energy Conversion, Photocatalysis and Environmental Remediation. *Energy Environ. Sci.* **2017**, *10*, 402–434. [CrossRef]
57. He, X.; Zhang, C. Recent Advances in Structure Design for Enhancing Photocatalysis. *J. Mater. Sci.* **2019**, *54*, 8831–8851. [CrossRef]
58. Lin, J.; Yu, J.C. An Investigation on Photocatalytic Activities of mixed TiO_2-Rare Earth Oxides for the Oxidation of Acetone in Air. *J. Photochem. Photobiol. A* **1998**, *116*, 63–67. [CrossRef]
59. Girish Kumar, S.; Kavitha, R. Lanthanide Ions doped ZnO based Photocatalysts. *Sep. Purif. Technol.* **2021**, *274*, 118853. [CrossRef]
60. Mazierski, P.; Lisowski, W.; Grzyb, T.; Winiarski, M.J.; Klimczuk, T.; Mikołajczyk, A.; Flisikowski, J.; Hirsch, A.; Kołakowska, A.; Puzyn, T.; et al. Enhanced Photocatalytic Properties of Lanthanide-TiO_2 Nanotubes: An Experimental and Theoretical Study. *Appl. Catal. B* **2017**, *205*, 376–385. [CrossRef]
61. Mazierski, P.; Mikolajczyk, A.; Bajorowicz, B.; Malankowska, A.; Zaleska-Medynska, A.; Nadolna, J. The Role of Lanthanides in TiO_2-based Photocatalysis: A Review. *Appl. Catal. B* **2018**, *233*, 301–317. [CrossRef]
62. Saqib, N.U.; Adnan, R.; Shah, I. A Mini-Review on Rare Earth Metal-doped TiO_2 for Photocatalytic Remediation of Wastewater. *Environ. Sci. Pollut. Res. Int.* **2016**, *23*, 15941–15951. [CrossRef]
63. Štengl, V.; Bakardjieva, S.; Murafa, N. Preparation and Photocatalytic Activity of Rare Earth doped TiO_2 Nanoparticles. *Mater. Chem. Phys.* **2009**, *114*, 217–226. [CrossRef]
64. Bingham, S.; Daoud, W.A. Recent advances in making nano-sized TiO2visible-light active through rare-earth metal doping. *J. Mater. Chem.* **2011**, *21*, 2041–2050. [CrossRef]
65. Weber, A.S.; Grady, A.M.; Koodali, R.T. Lanthanide Modified Semiconductor Photocatalysts. *Catal. Sci. Technol.* **2012**, *2*, 683. [CrossRef]
66. Goryacheva, O.A.; Beloglazova, N.V.; Vostrikova, A.M.; Pozharov, M.V.; Sobolev, A.M.; Goryacheva, I.Y. Lanthanide-to-Quantum Dot Förster Resonance Energy Transfer (FRET): Application for Immunoassay. *Talanta* **2017**, *164*, 377–385. [CrossRef]
67. Carnall, W.T. *Handbook on the Physics and Chemistry of Rare Earths*; Elsevier: Amsterdam, The Netherlands, 1979; Volume 3, pp. 171–208.
68. Zhang, W.; Yang, S.; Li, J.; Gao, W.; Deng, Y.; Dong, W.; Zhao, C.; Lu, G. Visible-to-Ultraviolet Upconvertion: Energy Transfer, Material Matrix, and Synthesis Strategies. *Appl. Catal. B* **2017**, *206*, 89–103. [CrossRef]
69. Emeline, A.V.; Kuznetsov, V.N.; Ryabchuk, V.K.; Serpone, N. On the way to the creation of next generation photoactive materials. *Environ. Sci. Pollut. Res.* **2012**, *19*, 3666–3675. [CrossRef] [PubMed]

70. Serpone, N.; Emeline, A.V. Semiconductor Photocatalysis—Past, Present, and Future Outlook. *J. Phys. Chem. Lett.* **2012**, *3*, 673–677. [CrossRef]
71. Gionco, C.; Paganini, M.C.; Chiesa, M.; Maurelli, S.; Livraghi, S.; Giamello, E. Cerium Doped Zirconium Dioxide as a Potential New Photocatalytic Material. The Role of the Preparation Method on the Properties of the Material. *Appl. Catal. A* **2015**, *504*, 338–343. [CrossRef]
72. Gionco, C.; Paganini, M.C.; Giamello, E.; Burgess, R.; Di Valentin, C.; Pacchioni, G. Cerium-Doped Zirconium Dioxide, a Visible-Light-Sensitive Photoactive Material of Third Generation. *J. Phys. Chem. Lett.* **2014**, *5*, 447–451. [CrossRef]
73. Gionco, C.; Paganini, M.C.; Giamello, E.; Sacco, O.; Vaiano, V.; Sannino, D. Rare Earth Oxides in Zirconium Dioxide: How to Turn a Wide Band Gap Metal Oxide into a Visible Light Active Photocatalyst. *J. Energy Chem.* **2016**, *26*, 270–276. [CrossRef]
74. Trovarelli, A. Catalytic Properties of Ceria and CeO_2-Containing Materials. *Cat. Rev.* **1996**, *38*, 439–520. [CrossRef]
75. Gorte, R.J. Ceria in Catalysis: From Automotive Applications to the Water-Gas Shift Reaction. *AIChE J.* **2010**, *56*, 1126–1135. [CrossRef]
76. Da Silva, A.M.; de Souza, K.R.; Mattos, L.V.; Jacobs, G.; Davis, B.H.; Noronha, F.B. The Effect of Support Reducibility on the Stability of Co/CeO_2 for the Oxidative Steam Reforming of Ethanol. *Catal. Today* **2011**, *164*, 234–239. [CrossRef]
77. Wu, Z.; Li, M.; Overbury, S.H. On the Structure Dependence of CO Oxidation over CeO_2 Nanocrystals with Well-Defined Surface Planes. *J. Catal.* **2012**, *285*, 61–73. [CrossRef]
78. Torrente-Murciano, L.; Gilbank, A.; Puertolas, B.; Garcia, T.; Solsona, B.; Chadwick, D. Shape-Dependency Activity of Nanostructured CeO_2 in the Total Oxidation of Polycyclic Aromatic Hydrocarbons. *Appl. Catal. B* **2013**, *132-133*, 116–122. [CrossRef]
79. Pinaeva, L.G.; Sadovskaya, E.M.; Ivanova, Y.A.; Kuznetsova, T.G.; Prosvirin, I.P.; Sadykov, V.A.; Schuurman, Y.; van Veen, A.C.; Mirodatos, C. Water Gas Shift and Partial Oxidation of CH_4 over CeO_2–ZrO_2(–La_2O_3) and Pt/CeO_2–ZrO_2(–La_2O_3): Performance under Transient Conditions. *Chem. Eng. J.* **2014**, *257*, 281–291. [CrossRef]
80. Wuilloud, E.; Delley, B.; Schneider, W.D.; Baer, Y. Spectroscopic Evidence for Localized and Extended f-Symmetry States in CeO_2. *Phys. Rev. Lett.* **1984**, *53*, 202–205. [CrossRef]
81. Al Abri, R.; Al Marzouqi, F.; Kuvarega, A.T.; Meetani, M.A.; Al Kindy, S.M.Z.; Karthikeyan, S.; Kim, Y.; Selvaraj, R. Nanostructured Cerium-doped ZnO for Photocatalytic Degradation of Pharmaceuticals in Aqueous Solution. *J. Photochem. Photobiol. A* **2019**, *384*, 112065. [CrossRef]
82. Bechambi, O.; Jlaiel, L.; Najjar, W.; Sayadi, S. Photocatalytic Degradation of Bisphenol A in the Presence of Ce-ZnO: Evolution of Kinetics, Toxicity and Photodegradation Mechanism. *Mater. Chem. Phys.* **2016**, *173*, 95–105. [CrossRef]
83. Bechambi, O.; Touati, A.; Sayadi, S.; Najjar, W. Effect of Cerium Doping on the Textural, Structural and Optical Properties of Zinc Oxide: Role of Cerium and Hydrogen Peroxide to Enhance the Photocatalytic Degradation of Endocrine Disrupting Compounds. *Mater. Sci. Semicond. Process.* **2015**, *39*, 807–816. [CrossRef]
84. Ha, L.T.V.; Dai, L.M.; Lim, D.T.; Nhiem, D.N.; Pham, N.N. Pure and Cerium-doped Zinc Oxides: Hydrothermal Synthesis and Photocatalytic Degradation of Methylene Blue under Visible Light Rradiation. *J. Chin. Chem. Soc.* **2020**, *67*, 1631–1643. [CrossRef]
85. Chang, C.-J.; Lin, C.-Y.; Hsu, M.-H. Enhanced Photocatalytic Activity of Ce-doped ZnO Nanorods under UV and Visible Light. *J. Taiwan Inst. Chem. Eng.* **2014**, *45*, 1954–1963. [CrossRef]
86. Sin, J.C.; Lamb, S.M.; Leec, K.T.; Mohamed, A.R. Preparation of Cerium-Doped ZnO Hierarchical Micro/Nanospheres with Enhanced Photocatalytic Performance for Phenol Degradation under Visible Light. *J. Mol. Catal. A Chem.* **2015**, *409*, 1–10. [CrossRef]
87. Jiang, J.; Zhang, K.; Chen, X.; Zhao, F.; Xie, T.; Wang, D.; Lin, Y. Porous Ce-doped ZnO Hollow Sphere with Enhanced Photodegradation Activity for Artificial Waste Water. *J. Alloys Compd.* **2017**, *699*, 907–913. [CrossRef]
88. Raza, W.; Haque, M.M.; Muneer, M. Synthesis of Visible Light driven ZnO: Characterization and Photocatalytic Performance. *Appl. Surf. Sci.* **2014**, *322*, 215–224. [CrossRef]
89. Rezaei, M.; Habibi-Yangjeh, A. Simple and Large Scale Refluxing Method for Preparation of Ce-doped ZnO Nanostructures as highly Efficient Photocatalyst. *Appl. Surf. Sci.* **2013**, *265*, 591–596. [CrossRef]
90. Elias, M.; Amin, M.K.; Firoz, S.H.; Hossain, M.A.; Akter, S.; Hossain, M.A.; Uddin, M.N.; Siddiquey, I.A. Microwave-Assisted Synthesis of Ce-doped ZnO/CNT Composite with Enhanced Photo-Catalytic Activity. *Ceram. Int.* **2017**, *43*, 84–91. [CrossRef]
91. Elias, M.; Uddin, M.N.; Hossain, M.A.; Saha, J.K.; Siddiquey, I.A.; Sarker, D.R.; Diba, Z.R.; Uddin, J.; Rashid Choudhury, M.H.; Firoz, S.H. An Experimental and Theoretical Study of the Effect of Ce doping in ZnO/CNT Composite Thin Film with Enhanced Visible Light Photo-Catalysis. *Int. J. Hydrogen Energy* **2019**, *44*, 20068–20078. [CrossRef]
92. Saad, A.M.; Abukhadra, M.R.; Abdel-Kader Ahmed, S.; Elzanaty, A.M.; Mady, A.H.; Betiha, M.A.; Shim, J.J.; Rabie, A.M. Photocatalytic Degradation of Malachite Green Dye using Chitosan supported ZnO and Ce-ZnO Nano-flowers under Visible Light. *J. Environ. Manage.* **2020**, *258*, 110043. [CrossRef]
93. Kaneva, N.; Bojinova, A.; Papazova, K.; Dimitrov, D. Photocatalytic Purification of Dye Contaminated Sea Water by Lanthanide (La^{3+}, Ce^{3+}, Eu^{3+}) modified ZnO. *Catal. Today* **2015**, *252*, 113–119. [CrossRef]
94. Karunakaran, C.; Gomathisankar, P.; Manikandan, G. Preparation and Characterization of Antimicrobial Ce-doped ZnO Nanoparticles for Photocatalytic Detoxification of Cyanide. *Mater. Chem. Phys.* **2010**, *123*, 585–594. [CrossRef]
95. Wang, L.; Ji, Z.; Lin, J.; Li, P. Preparation and Optical and Photocatalytic Properties of Ce-doped ZnO Microstructures by Simple Solution Method. *Mater. Sci. Semicond. Process.* **2017**, *71*, 401–408. [CrossRef]

96. Yayapao, O.; Thongtem, S.; Phuruangrat, A.; Thongtem, T. Sonochemical Synthesis, Photocatalysis and Photonic Properties of 3% Ce-doped ZnO Nanoneedles. *Ceram. Int.* **2013**, *39*, S563–S568. [CrossRef]
97. He, L.; Meng, J.; Feng, J.; Yao, F.; Zhang, L.; Zhang, Z.; Liu, X.; Zhang, H. Investigation of 4f-Related Electronic Transitions of Rare-Earth Doped ZnO Luminescent Materials: Insights from First-Principles Calculations. *ChemPhysChem* **2020**, *21*, 51–58. [CrossRef]
98. Sukriti, K.; Chand, P.; Singh, V.; Kumar, D. Rapid Visible Light-Driven Photocatalytic Degradation using Ce-doped ZnO Nanocatalysts. *Vacuum* **2020**, *178*, 109364. [CrossRef]
99. Lutterotti, L. Total Pattern Fitting for the Combined Size–Strain–Stress–Texture Determination in Thin Film Diffraction. *Nucl. Instrum. Methods Phys. Res. Sect. B* **2010**, *268*, 334–340. [CrossRef]
100. Kumar, M.; Chauhan, M.S.; Akhtar, M.S.; Umar, A. Effect of Cerium Ions in Ce-Doped ZnO Nanostructures on their Photocatalytic and Picric Acid Chemical Sensing. *Ceram. Int.* **2021**, *47*, 3089–3098. [CrossRef]
101. Cerrato, E.; Gionco, C.; Paganini, M.C.; Giamello, E.; Albanese, E.; Pacchioni, G. Origin of Visible Light Photoactivity of the CeO_2/ZnO Heterojunction. *ACS Appl. Energy Mat.* **2018**, *1*, 4247–4260. [CrossRef]
102. Ahmad, M.; Ahmed, E.; Zafar, F.; Khalid, N.R.; Niaz, N.A.; Hafeez, A.; Ikram, M.; Khan, M.A.; Hong, Z. Enhanced photocatalytic activity of Ce-doped ZnO nanopowders synthesized by combustion method. *J. Rare Earths* **2015**, *33*, 255–262. [CrossRef]
103. Ahmad, I.; Akhtar, M.S.; Ahmed, E.; Ahmad, M. Aluminium and Cerium co-doped ZnO Nanoparticles: Facile and Inexpensive Synthesis and Visible Light Photocatalytic Performances. *J. Rare Earths* **2021**, *39*, 151–159. [CrossRef]
104. Cerrato, E.; Gionco, C.; Berruti, I.; Sordello, F.; Calza, P.; Paganini, M.C. Rare earth ions doped ZnO: Synthesis, characterization and preliminary photoactivity assessment. *J. Solid State Chem.* **2018**, *264*, 42–47. [CrossRef]
105. Calza, P.; Gionco, C.; Giletta, M.; Kalaboka, M.; Sakkas, V.A.; Albanis, T.; Paganini, M.C. Assessment of the Abatement of Acelsulfame K using Cerium doped ZnO as Photocatalyst. *J. Hazard. Mater.* **2017**, *323*, 471–477. [CrossRef] [PubMed]
106. Chaker, H.; Attar, A.E.; Djennas, M.; Fourmentin, S. A Statistical Modeling-Optimization Approach for Efficiency Photocatalytic Degradation of Textile Azo Dye using Cerium-doped Mesoporous ZnO: A central Composite Design in Response Surface Methodology. *Chem. Eng. Res. Des.* **2021**, *171*, 198–212. [CrossRef]
107. Faisal, M.; Ismail, A.A.; Ibrahim, A.A.; Bouzid, H.; Al-Sayari, S.A. Highly Efficient Photocatalyst based on Ce doped ZnO Nanorods: Controllable Synthesis and Enhanced Photocatalytic Activity. *Chem. Eng. J.* **2013**, *229*, 225–233. [CrossRef]
108. Paganini, M.C.; Dalmasso, D.; Gionco, C.; Polliotto, V.; Mantilleri, L.; Calza, P. Beyond TiO_2: Cerium-Doped Zinc Oxide as a New Photocatalyst for the Photodegradation of Persistent Pollutants. *ChemistrySelect* **2016**, *1*, 3377–3383. [CrossRef]
109. Caregnato, P.; Espinosa Jiménez, K.R.; Villabrille, P.I. Ce-doped ZnO as Photocatalyst for Carbamazepine Degradation. *Catal. Today* **2021**, *372*, 183–190. [CrossRef]
110. Bazta, O.; Urbieta, A.; Trasobares, S.; Piqueras, J.; Fernández, P.; Addou, M.; Calvino, J.J.; Hungría, A.B. In-Depth Structural and Optical Analysis of Ce-modified ZnO Nanopowders with Enhanced Photocatalytic Activity Prepared by Microwave-Assisted Hydrothermal Method. *Catalysts* **2020**, *10*, 551. [CrossRef]
111. Ha, L.T.V.; Dai, L.M.; Nhiem, D.N.; Van Cuong, N. Enhanced Visible-Light Photocatalytic Activity of C/Ce-Codoped ZnO Nanoellipsoids Synthesized by Hydrothermal Method. *J. Electron. Mater.* **2016**, *45*, 4215–4220. [CrossRef]
112. Liang, Y.; Guo, N.; Li, L.; Li, R.; Ji, G.; Gan, S. Preparation of Porous 3D Ce-doped ZnO Microflowers with Enhanced Photocatalytic Performance. *RSC Adv.* **2015**, *5*, 59887–59894. [CrossRef]
113. Kardeş, M.; Başaran Dindaş, G.; Yatmaz, H.C.; Dizge, N.; Öztürk, K. CBD Grown Pure and Ce-doped ZnO Nanorods: Comparison of their Photocatalytic Degrading Efficiencies on AR88 Azo Dye under Visible Light Irradiation. *Colloids Surf. A* **2020**, *607*, 125451. [CrossRef]
114. He, W.; Zhao, H.; Jia, H.; Yin, J.-J.; Zheng, Z. Determination of Reactive Oxygen Species from ZnO Micro-Nano Structures with Shape-Dependent Photocatalytic Activity. *Mater. Res. Bull.* **2014**, *53*, 246–250. [CrossRef]
115. Wang, C.; Fan, H.; Ren, X.; Fang, J. Room Temperature Synthesis and Enhanced Photocatalytic Property of CeO_2/ZnO Heterostructures. *Appl. Phys. A* **2018**, *124*, 99. [CrossRef]
116. Parangusan, H.; Ponnamma, D.; Al-Maadeed, M.A.A. Effect of Cerium Doping on the Optical and Photocatalytic Properties of ZnO Nanoflowers. *Bull. Mater. Sci.* **2019**, *42*, 179. [CrossRef]
117. Pathak, T.K.; Coetsee-Hugo, E.; Swart, H.C.; Swart, C.W.; Kroon, R.E. Preparation and Characterization of Ce doped ZnO Nanomaterial for Photocatalytic and Biological Applications. *Mater. Sci. Eng. B* **2020**, *261*, 114780. [CrossRef]
118. Rezaei, M.; Habibi-Yangjeh, A. Microwave-Assisted Preparation of Ce-doped ZnO Nanostructures as an Efficient Photocatalyst. *Mater. Lett.* **2013**, *110*, 53–56. [CrossRef]
119. Rodríguez-Peña, M.; Flores-Carrasco, G.; Urbieta, A.; Rabanal, M.E.; Fernández, P. Growth and Characterisation of ZnO Micro/Nanostructures doped with Cerium for Photocatalytic Degradation Applications. *J. Alloys Compd.* **2020**, *820*, 153146. [CrossRef]
120. Kannadasan, N.; Shanmugam, N.; Cholan, S.; Sathishkumar, K.; Viruthagiri, G.; Poonguzhali, R. The Effect of Ce^{4+} Incorporation on Structural, Morphological and Photocatalytic Characters of ZnO Nanoparticles. *Mater. Charact.* **2014**, *97*, 37–46. [CrossRef]
121. Sordello, F.; Berruti, I.; Gionco, C.; Paganini, M.C.; Calza, P.; Minero, C. Photocatalytic Performances of Rare Earth Element-Doped Zinc Oxide toward Pollutant Abatement in Water and Wastewater. *Appl. Catal. B* **2019**, *245*, 159–166. [CrossRef]

122. Fabbri, D.; Lopez-Munoz, M.J.; Daniele, A.; Medana, C.; Calza, P. Photocatalytic Abatement of Emerging Pollutants in Pure Water and Wastewater Effluent by TiO_2 and Ce-ZnO: Degradation Kinetics and Assessment of Transformation Products. *Photochem. Photobiol. Sci.* **2019**, *18*, 845–852. [CrossRef]
123. Bohle, D.S.; Spina, C.J. Cationic and Anionic Surface Binding Sites on Nanocrystalline Zinc Oxide: Surface Influence on Photoluminescence and Photocatalysis. *J. Am. Chem. Soc.* **2009**, *131*, 4397–4404. [CrossRef] [PubMed]
124. Al-Namshah, K.S.; Mariappan, S.M.; Shkir, M.; Hamdy, M.S. Photocatalytic Degradation Mechanism of Ce-loaded ZnO Catalysts Toward Methyl Green Dye Pollutant. *Appl. Phys. A Mater. Sci. Process.* **2021**, *127*, 452. [CrossRef]
125. Kumar, R.; Umar, A.; Kumar, G.; Akhtar, M.S.; Wang, Y.; Kim, S.H. Ce-doped ZnO Nanoparticles for Efficient Photocatalytic Degradation of direct Red-23 Dye. *Ceram. Int.* **2015**, *41*, 7773–7782. [CrossRef]
126. Lang, J.; Wang, J.; Zhang, Q.; Li, X.; Han, Q.; Wei, M.; Sui, Y.; Wang, D.; Yang, J. Chemical Precipitation Synthesis and Significant Enhancement in Photocatalytic Activity of Ce-doped ZnO Nanoparticles. *Ceram. Int.* **2016**, *42*, 14175–14181. [CrossRef]
127. Meshram, S.P.; Adhyapak, P.V.; Pardeshi, S.K.; Mulla, I.S.; Amalnerkar, D.P. Sonochemically generated Cerium doped ZnO Nanorods for highly Efficient Photocatalytic Dye Degradation. *Powder Technol.* **2017**, *318*, 120–127. [CrossRef]
128. Shen, Z.; Zhang, Q.; Yin, C.; Kang, S.; Jia, H.; Li, X.; Li, X.; Wang, Y.; Cui, L. Facile synthesis of 3D flower-like mesoporous Ce-ZnO at room temperature for the sunlight-driven photocatalytic degradations of RhB and phenol. *J. Colloid Interface Sci.* **2019**, *556*, 726–733. [CrossRef] [PubMed]
129. Ozawa, M. Role of Cerium–Zirconium Mixed Oxides as Catalysts for Car Pollution: A Short Review. *J. Alloys Compd.* **1998**, *275-277*, 886–890. [CrossRef]
130. Monte, R.D.; Kašpar, J. Nanostructured CeO_2–ZrO_2 Mixed Oxides. *J. Mater. Chem.* **2005**, *15*, 633–648. [CrossRef]
131. Devaiah, D.; Reddy, L.H.; Park, S.-E.; Reddy, B.M. Ceria–Zirconia Mixed Oxides: Synthetic Methods and Applications. *Cat. Rev.* **2018**, *60*, 177–277. [CrossRef]
132. Li, M.; Liu, Y.; Dong, L.; Shen, C.; Li, F.; Huang, M.; Ma, C.; Yang, B.; An, X.; Sand, W. Recent Advances on Photocatalytic Fuel Cell for Environmental Applications-The marriage of Photocatalysis and Fuel Cells. *Sci. Total Environ.* **2019**, *668*, 966–978. [CrossRef]
133. Paksoy, A.I.; Yassi Akdag, C.; Selen Caglayan, B.; Aksoylu, A.E. Kinetic and Mechanistic Features of Carbon Dioxide Reforming of Methane over Co-Ce/ZrO_2 Catalysts. *Int. J. Chem. Kinet.* **2019**, *51*, 138–145. [CrossRef]
134. Paganini, M.C.; Cerrato, E. Photoactive Systems based on Semiconducting Metal Oxides. In *Material Science in Photocatalysis*; Garcıa-Lopez, E.I., Palmisano, L., Eds.; Elsevier: Amsterdam, The Netherlands, 2021; Volume 1, pp. 221–234.
135. Gionco, C.; Hernández, S.; Castellino, M.; Gadhi, T.A.; Muñoz-Tabares, J.A.; Cerrato, E.; Tagliaferro, A.; Russo, N.; Paganini, M.C. Synthesis and Characterization of Ce and Er doped ZrO_2 Nanoparticles as Solar Light Driven Photocatalysts. *J. Alloys Compd.* **2019**, *775*, 896–904. [CrossRef]
136. Kucio, K.; Charmas, B.; Sydorchuk, V.; Khalameida, S.; Khyzhun, O. Synthesis and Modification of Ce-Zr Oxide Compositions as Photocatalysts. *Appl. Catal. A* **2020**, *603*, 117767. [CrossRef]
137. Wang, X.; Zhai, B.; Yang, M.; Han, W.; Shao, X. ZrO_2/CeO_2 Nanocomposite: Two step Synthesis, Microstructure, and Visible-Light Photocatalytic Activity. *Mater. Lett.* **2013**, *112*, 90–93. [CrossRef]
138. Zhang, C.; Lin, J. Visible-Light induced oxo-bridged Zr(IV)-O-Ce(III) Redox Centre in Tetragonal ZrO_2-CeO_2 Solid Solution for Degradation of Organic Pollutants. *Phys. Chem. Chem. Phys.* **2011**, *13*, 3896–3905. [CrossRef] [PubMed]
139. Hao, Y.; Li, L.; Zhang, J.; Luo, H.; Zhang, X.; Chen, E. Multilayer and Open Structure of Dendritic Crosslinked CeO_2-ZrO_2 Composite: Enhanced Photocatalytic Degradation and Water Splitting Performance. *Int. J. Hydrog. Energy* **2017**, *42*, 5916–5929. [CrossRef]
140. Bortot Coelho, F.E.; Gionco, C.; Paganini, M.C.; Calza, P.; Magnacca, G. Control of Membrane Fouling in Organics Filtration Using Ce-Doped Zirconia and Visible Light. *Nanomaterials* **2019**, *9*, 534. [CrossRef] [PubMed]
141. Pouretedal, H.R.; Tofangsazi, Z.; Keshavarz, M.H. Photocatalytic Activity of Mixture of ZrO_2/SnO_2, ZrO_2/CeO_2 and SnO_2/CeO_2 Nanoparticles. *J. Alloys Compd.* **2012**, *513*, 359–364. [CrossRef]
142. García-López, E.; Marcì, G.; Pomilla, F.R.; Paganini, M.C.; Gionco, C.; Giamello, E.; Palmisano, L. ZrO2 Based Materials as Photocatalysts for 2-Propanol Oxidation by using UV and Solar Light Irradiation and Tests for CO_2 Reduction. *Catal. Today* **2018**, *313*, 100–105. [CrossRef]
143. Hernandez, S.; Gionco, C.; Husak, T.; Castellino, M.; Munoz-Tabares, J.A.; Tolod, K.R.; Giamello, E.; Paganini, M.C.; Russo, N. Insights Into the Sunlight-Driven Water Oxidation by Ce and Er-Doped ZrO_2. *Front. Chem.* **2018**, *6*, 368. [CrossRef]
144. Franco, P.; Sacco, O.; De Marco, I.; Sannino, D.; Vaiano, V. Photocatalytic Degradation of Eriochrome Black-T Azo Dye Using Eu-Doped ZnO Prepared by Supercritical Antisolvent Precipitation Route: A Preliminary Investigation. *Top. Catal.* **2020**, *63*, 1193–1205. [CrossRef]
145. Bünzli, J.-C. Europium in the limelight. *Nat. Chem.* **2010**, *2*, 696. [CrossRef] [PubMed]
146. Kitai, A. *Luminescent Materials and Applications*; John Wiley & Sons: Hoboken, NJ, USA, 2008; Volume 25.
147. Katea, S.N.; Broqvist, P.; Kullgren, J.; Hemmer, E.; Westin, G. Fast, Low-Cost Synthesis of ZnO:Eu Nanosponges and the Nature of Ln Doping in ZnO. *Inorg. Chem.* **2020**, *59*, 7584–7602. [CrossRef] [PubMed]
148. Chandrasekhar, M.; Nagabhushana, H.; Vidya, Y.S.; Anantharaju, K.S.; Sharma, S.C.; Premkumar, H.B.; Prashantha, S.C.; Prasad, B.D.; Shivakumara, C.; Saraf, R.; et al. Synthesis of Eu3+-activated ZnO superstructures: Photoluminescence, Judd–Ofelt analysis and Sunlight photocatalytic properties. *J. Mol. Catal. A Chem.* **2015**, *409*, 26–41. [CrossRef]

149. Hernández-Carrillo, M.A.; Torres-Ricárdez, R.; García-Mendoza, M.F.; Ramírez-Morales, E.; Rojas-Blanco, L.; Díaz-Flores, L.L.; Sepúlveda-Palacios, G.E.; Paraguay-Delgado, F.; Pérez-Hernández, G. Eu-modified ZnO nanoparticles for applications in photocatalysis. *Catal. Today* **2020**, *349*, 191–197. [CrossRef]
150. Khataee, A.R.; Karimi, A.; Soltani, R.D.C.; Safarpour, M.; Hanifehpour, Y.; Joo, S.W. Europium-doped ZnO as a visible light responsive nanocatalyst: Sonochemical synthesis, characterization and response surface modeling of photocatalytic process. *Appl. Catal. A Gen.* **2014**, *488*, 160–170. [CrossRef]
151. Korake, P.V.; Kadam, A.N.; Garadkar, K.M. Photocatalytic activity of Eu3+-doped ZnO nanorods synthesized via microwave assisted technique. *J. Rare Earths* **2014**, *32*, 306–313. [CrossRef]
152. Poornaprakash, B.; Chalapathi, U.; Sekhar, M.C.; Rajendar, V.; Vattikuti, S.V.P.; Pratap Reddy, M.S.; Suh, Y.; Park, S.-H. Effect of Eu3+ on the morphology, structural, optical, magnetic, and photocatalytic properties of ZnO nanoparticles. *Superlattices Microstruct.* **2018**, *123*, 154–163. [CrossRef]
153. Sin, J.-C.; Lam, S.-M.; Satoshi, I.; Lee, K.-T.; Mohamed, A.R. Sunlight photocatalytic activity enhancement and mechanism of novel europium-doped ZnO hierarchical micro/nanospheres for degradation of phenol. *Appl. Catal. B Environ.* **2014**, *148-149*, 258–268. [CrossRef]
154. Trandafilović, L.V.; Jovanović, D.J.; Zhang, X.; Ptasińska, S.; Dramićanin, M.D. Enhanced photocatalytic degradation of methylene blue and methyl orange by ZnO:Eu nanoparticles. *Appl. Catal. B Environ.* **2017**, *203*, 740–752. [CrossRef]
155. Zong, Y.; Li, Z.; Wang, X.; Ma, J.; Men, Y. Synthesis and high photocatalytic activity of Eu-doped ZnO nanoparticles. *Ceram. Int.* **2014**, *40*, 10375–10382. [CrossRef]
156. Dash, D.; Panda, N.R.; Sahu, D. Photoluminescence and photocatalytic properties of europium doped ZnO nanoparticles. *Appl. Surf. Sci.* **2019**, *494*, 666–674. [CrossRef]
157. Babayevska, N.; Iatsunskyi, I.; Florczak, P.; Jarek, M.; Peplińska, B.; Jurga, S. Enhanced photodegradation activity of ZnO:Eu3+ and ZnO:Eu3+@Au 3D hierarchical structures. *J. Rare Earths* **2020**, *38*, 21–28. [CrossRef]
158. Marin, R.; Oussta, F.; Katea, S.N.; Prabhudev, S.; Botton, G.A.; Westin, G.; Hemmer, E. Europium-doped ZnO nanosponges–controlling optical properties and photocatalytic activity. *J. Mater. Chem. C* **2019**, *7*, 3909–3919. [CrossRef]
159. Ahmad, I.; Shoaib Akhtar, M.; Ahmed, E.; Ahmad, M.; Keller, V.; Qamar Khan, W.; Khalid, N.R. Rare earth co-doped ZnO photocatalysts: Solution combustion synthesis and environmental applications. *Sep. Purif. Technol.* **2020**, *237*, 116328. [CrossRef]
160. Ahmed, S.M.; Imam, H. Characterization and photocatalytic activity of Eu:ZnO & Au/Eu:ZnO nanoparticles prepared by laser ablation in water. *Mater. Sci. Semicond. Process.* **2020**, *115*, 105128. [CrossRef]
161. Sanchez Rayes, R.M.; Kumar, Y.; Cortes-Jácome, M.A.; Toledo Antonio, J.A.; Mathew, X.; Mathews, N.R. Effect of Eu Doping on the Physical, Photoluminescence, and Photocatalytic Characteristics of ZnO Thin Films Grown by Sol-Gel Method. *Phys. Status Solidi* **2017**, *214*, 1700229. [CrossRef]
162. Sin, J.-C.; Lam, S.-M. Hydrothermal synthesis of europium-doped flower-like ZnO hierarchical structures with enhanced sunlight photocatalytic degradation of phenol. *Mater. Lett.* **2016**, *182*, 223–226. [CrossRef]
163. Yang, L.; Wang, Z.; Zhang, Z.; Sun, Y.; Gao, M.; Yang, J.; Yan, Y. Surface effects on the optical and photocatalytic properties of graphene-like ZnO:Eu3+nanosheets. *J. Appl. Phys.* **2013**, *113*, 033514. [CrossRef]
164. Çiçek Bezir, N.; Evcin, A.; Kayali, R.; Özen, M.K.; Esen, K. Comparison of Five-Layered ZrO2 and Single-Layered Ce, Eu, and Dy-Doped ZrO2 Thin Films Prepared by Sol-Gel Spin Coating Method. *Acta Phys. Pol. A* **2017**, *132*, 612–616. [CrossRef]
165. Ghosh, P.; Priolkar, K.R.; Patra, A. Understanding the Local Structures of Eu and Zr in Eu2O3 Doped and Coated ZrO2 Nanocrystals by EXAFS Study. *J. Phys. Chem. C* **2007**, *111*, 571–578. [CrossRef]
166. Moon, B.K.; Kwon, I.M.; Jeong, J.H.; Kim, C.-S.; Yi, S.-S.; Kim, P.S.; Choi, H.; Kim, J.H. Synthesis and luminescence characteristics of Eu3+-doped ZrO2 nanoparticles. *J. Lumin.* **2007**, *122-123*, 855–857. [CrossRef]
167. Li, Z.; Liu, S.; Du, M.; Wang, J.; Srivastava, G.P.; Wang, M.; Wei, T.; Zou, Y.; Xiao, N.; Zhou, Q. Study of Synthesis and Photocatalytic Performance of the Monoclinic/Cubic Heterophase Junction of Rare Earth doped Zirconia. *J. Phys. Chem. Solids* **2021**, *159*, 110286. [CrossRef]
168. Du, W.; Zhu, Z.; Zhang, X.; Wang, D.; Liu, D.; Qian, X.; Du, J. RE/ZrO2 (RE=Sm, Eu) composite oxide nano-materials: Synthesis and applications in photocatalysis. *Mater. Res. Bull.* **2013**, *48*, 3735–3742. [CrossRef]
169. Agorku, E.S.; Kuvarega, A.T.; Mamba, B.B.; Pandey, A.C.; Mishra, A.K. Enhanced visible-light photocatalytic activity of multi-elements-doped ZrO2 for degradation of indigo carmine. *J. Rare Earths* **2015**, *33*, 498–506. [CrossRef]
170. Becker, P.; Olsson, A.; Simpson, J. *Erbium-Doped Fiber Amplifiers*; Elsevier: Amsterdam, The Netherlands, 1999; Volume 1, p. 460.
171. Srivastava, M.; Venkatasubramani, L.N.; Srinivasan, B.; Venkitesh, D. Nonlinearity-Assisted All-Optical Clock Recovery for Phase Modulated Lightwave Systems. *IEEE J. Sel. Top. Quantum Electron.* **2021**, *27*, 1–9. [CrossRef]
172. Castañeda-Contreras, J.; Marañón-Ruiz, V.F.; Chiu-Zárate, R.; Pérez-Ladrón de Guevara, H.; Rodriguez, R.; Michel-Uribe, C. Photocatalytic Activity of Erbium-doped TiO_2 Nanoparticles Immobilized in Macro-Porous Silica Films. *Mater. Res. Bull.* **2012**, *47*, 290–295. [CrossRef]
173. Bhatia, S.; Verma, N. Erbium-Doped Nanoparticles/Films for Enhancing Percentage Photodegradation of Direct Red-31 Dye. *J. Mater. Sci. Mater. Electron.* **2018**, *29*, 14960–14970. [CrossRef]
174. Chemingui, H.; Mzali, J.C.; Missaoui, T.; Konyar, M.; Smiri, M.; Cengiz Yatmaz, H.; Hafiane, A. Characteristics of Er-doped Zinc Oxide Layer: Application in Synthetic Dye Solution Color Removal. *Sep. Purif. Technol.* **2021**, *209*, 402–413. [CrossRef]

175. Divya, N.K.; Pradyumnan, P.P. Solid State Synthesis of Erbium doped ZnO with Excellent Photocatalytic Activity and Enhanced Visible Light Emission. *Mater. Sci. Semicond. Process.* **2016**, *41*, 428–435. [CrossRef]
176. Lee, G.-J.; Lin, C.-Y.; Wu, J.J. Preparation of Dumbbell-like Er/ZnO Microrods with Efficient Energy Upconversion for the Catalytic Degradation of Tartaric Acid in Water. *Top. Catal.* **2017**, *60*, 1359–1369. [CrossRef]
177. Narayanan, N.; Deepak, N.K. Amelioration of photocatalytic activity of ZnO thin films by Er doping. *J. Mater. Sci. Mater. Electron.* **2018**, *29*, 8774–8784. [CrossRef]
178. Pascariu, P.; Cojocaru, C.; Olaru, N.; Samoila, P.; Airinei, A.; Ignat, M.; Sacarescu, L.; Timpu, D. Novel Rare Earth (RE-La, Er, Sm) Metal doped ZnO Photocatalysts for Degradation of Congo-Red dye: Synthesis, Characterization and Kinetic Studies. *J. Environ. Manage.* **2019**, *239*, 225–234. [CrossRef] [PubMed]
179. Raza, W.; Faisal, S.M.; Owais, M.; Bahnemann, D.; Muneer, M. Facile Fabrication of Highly Efficient modified ZnO Photocatalyst with Enhanced Photocatalytic, Antibacterial and Anticancer Activity. *RSC Adv.* **2016**, *6*, 78335–78350. [CrossRef]
180. Yu, K.-s.; Shi, J.-y.; Zhang, Z.-l.; Liang, Y.-m.; Liu, W. Synthesis, Characterization, and Photocatalysis of ZnO and Er-Doped ZnO. *J. Nanomater.* **2013**, *2013*, 1–5. [CrossRef]
181. Zhang, Z.; Song, Y.; Wu, S.; Guo, J.; Zhang, Q.; Wang, J.; Yang, J.; Hua, Z.; Lang, J. Tuning the defects and luminescence of ZnO:(Er, Sm) nanoflakes for application in organic wastewater treatment. *J. Mater. Sci. Mater. Electron.* **2019**, *30*, 15869–15879. [CrossRef]
182. Sin, J.-C.; Lam, S.-M.; Lee, K.-T.; Mohamed, A.R. Fabrication of Erbium-doped Spherical-like ZnO Hierarchical Nanostructures with Enhanced Visible Light-Driven Photocatalytic Activity. *Mater. Lett.* **2013**, *91*, 1–4. [CrossRef]
183. Sowik, J.; Miodyńska, M.; Bajorowicz, B.; Mikolajczyk, A.; Lisowski, W.; Klimczuk, T.; Kaczor, D.; Zaleska Medynska, A.; Malankowska, A. Optical and Photocatalytic Properties of Rare Earth Metal-Modified ZnO Quantum Dots. *Appl. Surf. Sci.* **2019**, *464*, 651–663. [CrossRef]
184. Bhatia, S.; Verma, N.; Bedi, R.K. Optical Application of Er-doped ZnO Nanoparticles for Photodegradation of Direct red—31 dye. *Opt. Mater.* **2016**, *62*, 392–398. [CrossRef]
185. Zhou, J.; Liu, Q.; Feng, W.; Sun, Y.; Li, F. Upconversion Luminescent Materials: Advances and Applications. *Chem. Rev.* **2015**, *115*, 395–465. [CrossRef] [PubMed]
186. Wang, X.; Kong, X.; Yu, Y.; Sun, Y.; Zhang, H. Effect of Annealing on Upconversion Luminescence of ZnO:Er^{3+} Nanocrystals and High Thermal Sensitivity. *J. Phys. Chem. C* **2007**, *111*, 15119–15124. [CrossRef]
187. Tong, Y.; Lu, L.; Yang, X.; Wang, X. Characterization and their Photocatalytic Properties of $Ln_2Zr_2O_7$ (Ln=La, Nd, Sm, Dy, Er) Nanocrystals by Stearic Acid Method. *Solid State Sci.* **2008**, *10*, 1379–1383. [CrossRef]